Tunable Directional Couplers in Silicon-on-Insulator Technology Platform

Hasan Hoji

Department of Electrical & Computer Engineering

McGill University

Montreal, Canada

August 2024

A thesis submitted to McGill University in partial fulfillment of the requirements of the degree of

Master of Science.

Abstract

The rapid advancement of silicon photonics (SiPh) technology is reshaping the landscape of data transmission and processing. SiPh technology offers high data rates due to light-based transmission, which inherently has low latency. Additionally, SiPh is compatible with CMOS fabrication, allowing it to be produced using existing foundry infrastructure.

In recent years, there has been a growing trend towards performing computational tasks and vector-matrix multiplications using reconfigurable optical processors (ROPs). This shift is driven by the advantages of light-speed propagation within photonic chips and the superior energy efficiency they offer compared to traditional digital circuits. In parallel, optical data transmission can be enhanced using mode-division multiplexing (MDM). This involves developing on-chip MDM devices to exploit multiple optical modes. Both ROPs and MDM system applications face challenge due to fabrication process variations, which significantly impacting performance.

Fabrication errors in silicon-on-insulator (SOI) directional couplers, which are fundamental components in both ROPs and MDM systems, result in approximately $\pm 2\%$

to ±3% error in the splitting percentage. Simulation work reported in the literature show that 2% error in the 50:50 splitting percentage of directional couplers causes ROP accuracy to drop from 98% to 65% for a MNIST image classification task. This highlights the importance and potential of tunable couplers to compensate for these errors.

This thesis introduces a novel mode-selective tunable directional coupler (MS-TDC), alongside the development of a single-mode tunable directional coupler (SM-TDC). The MS-TDC uniquely offers the capability to selectively couple the first-order mode (TE1) without affecting the fundamental mode (TE0), which remains uncoupled. In contrast, the SM-TDC tunes the coupling for the fundamental mode (TE0). These couplers serve two purposes: addressing fabrication process variations affecting directional coupler splitters in ROPs, and enabling the selective tuning and (de)multiplexing of TE0 and TE1 modes in MDM systems.

Both proposed coupler designs incorporate silicon waveguide strip cross-sections with titanium tungsten (TiW) metal heaters placed above them, fabricated at the Applied Nanotools (ANT) foundry. The heaters adjust the refractive index in the coupling region, enabling fine control over the coupling ratio. Experimental testing involved using a C-band continuous tunable laser to sweep the wavelength and a DC power supply for electrical tuning. Experimental results with a 50 µm heater length demonstrate the ability to efficiently shift the 50:50 splitting wavelength by 0.43 nm/mW and 0.36 nm/mW for a coupling length of 6.5 µm in the SM-TDC and MS-TDC designs, respectively.

Experimentally the splitting percentage tunability reaches up to 10% with 45 mW applied electrical power. An improvement in tunability is achieved by increasing the coupling length. With a 23 µm coupling length, the MS-TDC mode selectivity reaches 25%. Simulation results suggest an increase to 35% with a 40 µm coupling length with 45 mW of applied power and using a heater length of 50 µm.

Abrégé

Les progrès rapides de la technologie de la photonique sur silicium (SiPh) transforment le paysage de la transmission et du traitement des données. La technologie SiPh offre des débits élevés grâce à la transmission par la lumière, qui présente intrinsèquement une faible latence. De plus, SiPh est compatible avec la fabrication CMOS, permettant sa production en utilisant les infrastructures de fonderie existantes.

Ces dernières années, on observe une tendance croissante à effectuer des tâches computationnelles et des multiplications vecteur-matrice en utilisant des processeurs optiques reconfigurables (ROP). Ce changement est motivé par les avantages de la propagation à la vitesse de la lumière au sein des puces photoniques et par leur efficacité énergétique supérieure par rapport aux circuits numériques traditionnels. Parallèlement, la transmission de données optiques peut être améliorée grâce au multiplexage par division de modes (MDM). Cela implique le développement de dispositifs MDM sur puce pour exploiter plusieurs modes optiques. Les applications des ROP et des systèmes MDM sont confrontées à des défis en raison des variations du processus de fabrication, ce qui affecte

considérablement les performances.

Les erreurs de fabrication dans les coupleurs directionnels en silicium sur isolant (SOI), qui sont des composants fondamentaux des systèmes ROP et MDM, entraînent une erreur d'environ ±2% à ±3% dans le pourcentage de répartition. Les travaux de simulation rapportés dans la littérature montrent qu'une erreur de 2% dans le pourcentage de répartition 50:50 des coupleurs directionnels fait chuter la précision des ROP de 98% à 65% pour une tâche de classification d'images MNIST. Cela souligne l'importance et le potentiel des coupleurs réglables pour compenser ces erreurs.

Cette thèse présente un nouveau coupleur directionnel accordable sélectif aux modes (MS-TDC), ainsi que le développement d'un coupleur directionnel accordable monomode (SM-TDC). Le MS-TDC offre la capacité unique de coupler sélectivement le mode de premier ordre (TE1) sans affecter le mode fondamental (TE0), qui reste découplé. En revanche, le SM-TDC ajuste le couplage pour le mode fondamental (TE0). Ces coupleurs ont deux objectifs : corriger les variations de processus de fabrication affectant les répartiteurs des coupleurs directionnels dans les processeurs optiques reconfigurables (ROP) et permettre l'accordage et le (dé)multiplexage sélectifs des modes TE0 et TE1 dans les systèmes de multiplexage en division de mode (MDM) sur puce.

Les deux conceptions de coupleurs proposées intègrent des guides d'ondes en silicium sous forme de sections transversales, avec des résistances chauffantes en tungstène-titane (TiW) placées au-dessus, fabriquées à la fonderie Applied Nanotools (ANT). Les

résistances chauffantes ajustent l'indice de réfraction dans la région de couplage, permettant ainsi un contrôle précis du ratio de couplage. Les tests expérimentaux ont impliqué l'utilisation d'un laser accordable en bande C pour balayer la longueur d'onde et d'une alimentation électrique en courant continu pour l'accordage électrique. Les résultats expérimentaux avec une longueur de chauffage de 50 µm démontrent la capacité à déplacer efficacement la longueur d'onde de répartition 50:50 de 0.43 nm/mW et 0.36 nm/mW pour une longueur de couplage de 6.5 µm dans les SM-TDC et MS-TDC, respectivement. Expérimentalement, la possibilité de réglage du pourcentage de répartition atteint 10% avec une puissance électrique appliquée de 45 mW. Une amélioration de la possibilité de réglage est obtenue en augmentant la longueur de couplage. Avec une longueur de couplage de 23 µm, la sélectivité de mode du MS-TDC atteint 25%. Les résultats de simulation suggèrent une augmentation à 35% avec une longueur de couplage de 40 µm avec une puissance appliquée de 45 mW et en utilisant une longueur de chauffage de 50 µm.

Acknowledgements

I would like to begin by expressing my profound gratitude to Almighty Allah for granting me the strength and patience to endure and successfully complete my M.Sc. studies. I extend my heartfelt appreciation to my thesis supervisor, Prof. Odile Liboiron-Ladouceur, for offering me the invaluable opportunity to join her esteemed research team. Her unique leadership style, characterized by providing the freedom to explore the world of photonics and choose my research field, has been a remarkable experience. Her wise guidance has kept me on the right track, enabling me to develop my skills and knowledge to new heights. Additionally, I wish to acknowledge and thank Dr. Bahaa Radi, whose recommendation played a crucial role in my connection with my thesis supervisor. His support and guidance throughout my academic journey have been immeasurable.

I am also indebted to the entire to my esteemed colleagues on the "Photonic Datacom team" for their invaluable support and collaboration throughout my journey. In particular, I want to express my sincere appreciation to Dr. Kaveh (Hassan) Rahbardar Mojaver for his exceptional help and guidance during the paper writing and publication process. I am also

deeply thankful to S. Mohammad Reza Safaee for introducing me to the lab equipments and providing essential training.

I wholeheartedly dedicate all of my achievements to my beloved family. To my dear wife, Rama Alamleh, I am profoundly grateful for her unwavering stand beside me, her endless support, and her boundless patience. To my dear mother, I owe a debt of gratitude for her sincere prayers and warm emotions.

Contents

1 Introduction **1**

1.1 SiPh for Reconfigurable Optical Processors 2

1.2 SiPh for Mode Division Multiplexing 4

1.3 Motivations 5

1.4 Thesis Contributions 8

1.5 Thesis Organization 9

2 Background **11**

2.1 Optical Waveguides in Silicon-on-Insulator 11

2.1.1 Fabrication Process 12

2.1.2 Waveguide Optical Modes 14

2.2 Tuning Using Heaters 15

2.2.1 Thermo-optic Effect 15

2.2.2 Titanium Tungsten Thermal Properties 17

2.2.3 Metal Heater Resistivity 19

2.2.4 Power Dissipation in Metal Heater 20

2.3 Directional Couplers 22

2.3.1 Supermode Theory Approach 22
2.3.2 Impact of the Coupler Gap Separation 28
2.4 Mach-Zehnder Interferometer 30
2.4.1 MZIs in Reconfigurable Optical Processors 32
2.4.2 Impact of Imperfect MZI Splitters on ROPs 37
2.5 Summary 40

3 Single-Mode Tunable Directional Coupler 42
3.1 Design and Simulation 45
3.2 Experimental Setup 52
3.3 Experimental Results 54
3.4 Summary 58

4 Mode-Selective Tunable Directional Coupler 61
4.1 Design and Simulation 63
4.2 Experimental Setup 68
4.3 Experimental Results 70
4.4 Future Work 74
4.4.1 TE0 Mode Selective 3 dB Splitter 75
4.4.2 Both Modes 3 dB Splitter 77
4.5 Summary 78

5 Conclusion 80

List of Figures

1.1 4×4 MZI-based reconfigurable optical processor based on the Reck topology (adopted from [3]) © by F. Shokraneh, used under CC BY 4.0. 3

2.1 Schematic diagram illustrating the cross-sectional dimensions of ANT photonics chips (dimensions not to scale). 13

2.2 Simulation conducted in Ansys/Lumerical MODE of the effective index of the waveguide modes versus the width of a strip waveguide with a height of 220 nm, performed at a wavelength of 1550 nm. The horizontal dashed line represents the refractive index for the waveguide cladding (SiO_2). 15

2.3 Change in the refractive index with wavelengths for silicon at different temperatures using Sellmeier equation. 16

2.4 Change in temperature relative to 300 K of the coupling waveguides as a function of applied electrical power (P) for a 6 µm coupling length in a SM-TDC, considering different combinations of heater widths (W_{TiW}) and lengths (L_{TiW}). The horizontal dashed line represents the temperature rise of the coupling waveguides at metal failure. 21

2.5 Schematic of a coupler with two straight parallel strip waveguides, with the direction of the injected optical signal indicated. The waveguide width (W_{wg}) is 500 nm for single-mode TDC and 800 nm for mode-selective TDC (dimensions not to scale). 24

2.6 Electric field intensity distribution (E_y) for the TE0 mode and its supermodes for a directional coupler: real part for (a) the symmetric supermode and (b) the asymmetric supermode, cross-section of the real part along the z-axis for (c) the symmetric supermode and (d) the asymmetric supermode, (e) real part for the resultant TE0 mode obtained by vectorial summation of the symmetric and symmetric modes, (f) cross-section of the real part along the z-axis for the resultant TE0 mode in (e). 25

2.7 Electric field intensity distribution (E_y) for TE1 mode and its supermodes of a directional coupler: real part for (a) the symmetric supermode and (b) the asymmetric supermode, cross-section of the real part along the z-axis for (c) the symmetric supermode and (d) the asymmetric supermode, (e) real part for the resultant TE1 mode obtained by vectorial summation of the symmetric and symmetric modes, (f) cross-section of the real part along the z-axis for the resultant TE1 mode in (e). 28

2.8 Optical transmission crossover length versus coupler gap at 1550 nm and 800 × 220 nm^2 waveguides: (a) TE0 mode and (b) TE1 mode. 30

2.9 A 2×2 MZI building block with phase shifters denoted by θ and ϕ, (adopted from [3]) © by F. Shokraneh, used under CC BY 4.0. 31

2.10 MNIST classification accuracy for an 8×8 MZI-based topology as a function of phase shifters error and beamsplitters error (adopted from [7]) © 2019 Optical Society of America under the terms of the OSA Open Access Publishing Agreement. 33

2.11 Four MZI mesh topologies: (a) 4×4 Reck, (b) 4×4 Clements, (c) 8×8 Reck, (d) 8×8 Clements. Each numbered blue rectangle symbolizes an MZI, and each red number indicates the corresponding index on their diagonal matrix. The yellow and gray rectangles highlight examples of horizontal and vertical layers, respectively. 35

3.1 Schematic diagram of the designed TDC with its dimensions in the SOI technology platform, where L_{TiW} and W_{TiW} represent the length and width of the heater, respectively, and L_{TDC}, W_{TDC}, and Gap_{TDC} denote the coupling length, width, and gap of the coupler, respectively (dimensions not to scale). 46

3.2 Simulation of crossover length of the TE0 mode versus coupler gap at 1550 nm for a 500 $\times$ 220 nm^2 waveguide. 47

3.3 Simulation of the optical power transmission versus coupling length at a wavelength of 1550 nm for a SM-TDC with a 100 nm coupling gap. 48

3.4 Simulation of the coupling length required for a 50:50 splitting versus wavelength for a SM-TDC. Highlighted are the desired 50:50 splitting point at a wavelength of 1550 nm, and the designed 50:50 splitting point at a wavelength of 1532 nm, corresponding to coupling lengths of 5.6 µm and 6 µm, respectively. 49

3.5 Simulation of optical power transmission versus wavelength for a SM-TDC with a 6 µm coupling length at different power levels (0 mW and 47 mW) for a heater length of 50 µm. 50

3.6 Experimental setup for a SM-TDC. 53

3.7 Wavelength shift ($\Delta\lambda$) of the 50:50 splitting ratio as a function of the applied electrical power for a coupling length of 6.5 µm, for two different heater designs. 55

3.8 Measured change in the splitting ratio as a function of wavelength under two conditions: without the application of electrical power and with 20 mW of power applied, (a) for the SM-TDC with a coupling length of 6.5 µm, and heater dimensions of 3 µm in width and 50 µm in length; (b) for the SM-TDC with a coupling length of 5.5 µm, and heater dimensions of 3 µm in width and 100 µm in length. 56

3.9 Measured change in the splitting ratio of the SM-TDC as a function of applied electrical power at a specific wavelength. Configuration (a) corresponds to a coupling length of 6.5 µm, with a heater width and length of 3 µm and 50 µm, respectively, at a wavelength of 1511 nm. Configuration (b) represents a coupling length of 5.5 µm, featuring a heater width and length of 3 µm and 100 µm, respectively, at a wavelength of 1550 nm. 58

4.1 Schematic diagram of the designed MS-TDC with its dimensions in the SOI technology platform, where L_{TiW} and W_{TiW} represent the length and width of the heater, respectively, and L_{TDC} denotes the coupling length of the coupler. The table data represent the modes propagating in that port with their power transmission percentage when L_{TDC}= 30 µm (dimensions not to scale). . . . 62

4.2 Simulation of optical transmission versus electrical power applied to the MS-TDC, indicating the change in temperature of the coupling waveguide relative to 300 K with a coupling length of 30 µm and a gap of 160 nm at 1550 nm for two modes: (a) TE0 mode, (b) TE1 mode. 63

4.3 Simulation of optical power transmission versus coupling length at a wavelength at 1550 nm with a 160 nm coupling gap for MS-TDC: (a) TE0 mode, (b) TE1 mode. 64

4.4 Simulation of the electric field distribution in MS-TDC couplers for three different coupling lengths: 5.6 µm (left column), 13.5 µm (middle column), and 22 µm (right column). The top row shows the distribution for the TE0 mode, while the bottom row shows the distribution for the TE1 mode. . . . 66

4.5 Schematic of the TE mode (de)multiplexer (dimensions not to scale). 68

4.6 Schematic displays the TE0 and TE1 modes conversion and (de)multiplexing through the measuring circuit components. 69

4.7 The full schematic of the MS-TDC measuring circuit. 70

4.8 Wavelength shift ($\Delta\lambda$) of the 50:50 splitting ratio for TE1 mode as a function of applied electrical power for coupling lengths of 6.5 µm and 23 µm. The heater length is 50 µm and the width is 4 µm. 72

4.9 Measured change in the splitting ratio as a function of wavelength for two MS-TDC designs under two conditions: without the application of electrical power, and with the application of power needed for 50:50 splitting to reach 1550 nm, using heater dimensions of 4 µm in width and 50 µm in length. The measurements are conducted for both TE0 and TE1 modes, and include data for (a) a coupling length of 6.5 µm, as well as for (b) a coupling length of 23 µm. 73

4.10 Measured change in the splitting ratio of the MS-TDC with respect to applied electrical power at a specific wavelength, using a heater with dimensions of 4 µm width and 50 µm length. Configuration (a) corresponds to a coupling length of 6.5 µm at 1533 nm. Configuration (b) represents a coupling length of 23 µm at 1550 nm. 74

4.11 Simulations of transmission for a TDC with a 110 nm coupling gap and 810 × 220 nm^2 waveguides at 1550 nm: (a,b) versus coupling length for TE0 and TE1 modes, respectively, and (c,d) versus power for a coupling length of 47 µm for TE0 and TE1 modes, respectively. 77

List of Tables

1.1 Comparison of directional couplers for MDM systems. 7

2.1 Phase value for a practical example for a 4×4 Reck topology (units in radians). 37

3.1 Power required to shift the 50:50 splitting point to a wavelength of 1550 nm for 6 µm SM-TDC. 52

4.1 Power requirements for the MS-TDC to shift the 50:50 splitting point for coupling lengths of 6 µm and 23 µm from 1541 nm to 1550 nm, and to shift the full coupling point for a 15 µm coupling length of the TE1 mode from 1540 nm to 1550 nm, for different heater lengths. 67

4.2 Multi-mode directional coupler designs, where the splitting ratio is represented as a ratio of the through port over the cross port. 75

List of Acronyms

AI	Artificial Intelligence
ANT	Applied Nanotools Inc.
CMOS	Complementary Metal-Oxide-Semiconductor
CW	Continuous Wave
DC	Directional Coupler
DMZI	Dual Mach-Zehnder Interferometer
DUT	Device Under Test
EBL	Electron Beam Lithography
FDE	Finite Difference Eigenmode
FDTD	Finite-Difference Time-Domain
FMF	Few-Mode Fiber
ICP-RIE	Inductively-Coupled-Plasma Reactive Ion Etching
MDM	Mode Division Multiplexing
MEMS	Micro-Electromechanical Systems

MMI	Multimode Interference
MS-TDC	Mode Selective Tunable Directional Coupler
MZI	Mach-Zehnder Interferometer
PBS	Polarization Beam Splitter
PCM	Phase-change Material
PECVD	Plasma-enhanced Chemical Vapor Deposition
ROP	Reconfigurable Optical Processor
Si	Bulk Silicon
SiO_2	Silicon Dioxide
SiPh	Silicon Photonic
SMF	Single-Mode Fiber
SM-TDC	Single-Mode Tunable Directional Coupler
SOI	Silicon-on-Insulator
TDC	Tunable Directional Coupler
TDM	Time Division Multiplexing
TE	Transverse Electric Mode
TE0	Fundamental Transverse Electric Mode
TE1	First-order Transverse Electric Mode
TiW	Titanium Tungsten
TM0	Fundamental Transverse Magnetic Mode

TOC	Thermo-optic Coefficient
WDM	Wavelength Division Multiplexing

Chapter 1

Introduction

In recent years, the landscape of technology has undergone rapid transformations, driven by advancements in image processing, quantum computing, and the realm of artificial intelligence (AI) systems. This surge brings to light a formidable challenge: the urgency to efficiently and precisely handle this burgeoning data volume.

Traditionally, high-speed processing units have primarily relied on electronic devices. However, this dependence imposes limitations that become more apparent as data overload persists. Challenges such as large power consumption, limited parallelism, and the inevitable ceiling on processing speed underscore the need for novel solutions.

In response to these pressing constraints, optical processors has come forward as a possible solution. These optical processors can overcome the difficulties encountered by electronic processors, leveraging advantages such as lower power consumption, high-speed

processing enabled by light propagation in photonic chips, and inherently parallel processing capabilities. However, optical processing still struggle with its own set of challenges, particularly related to fabrication deviations impacting the optical devices employed in these processors. This thesis aims deeper into some of these challenges and proposes potential solutions to address them.

1.1 SiPh for Reconfigurable Optical Processors

Reconfigurable optical processors (ROPs) have gained attention in the world of photonics. They have shown promise in various fields such as neural networks [1] and quantum computing [2]. The primary advantages of ROPs lie in their ability to execute computational tasks, such as matrix multiplications, at the speed of light propagation within the photonic chip, with better energy efficiency compared to traditional digital circuits [3–5].

Some proposed ROPs are based on Mach-Zehnder interferometers (MZIs) as the building blocks. By designing MZI-based photonic circuits, these processors enable intricate matrix multiplications. One of the first MZI-based architectural concepts was introduced by Reck *et al.* in 1994 [6], where a triangular array of MZI elements created a 4×4 configuration to form a ROP. The topology enables the generation of a 4×4 linear transformation matrix, relating its outputs to its inputs as shown in Figure 1.1 and described by Equation 1.1.

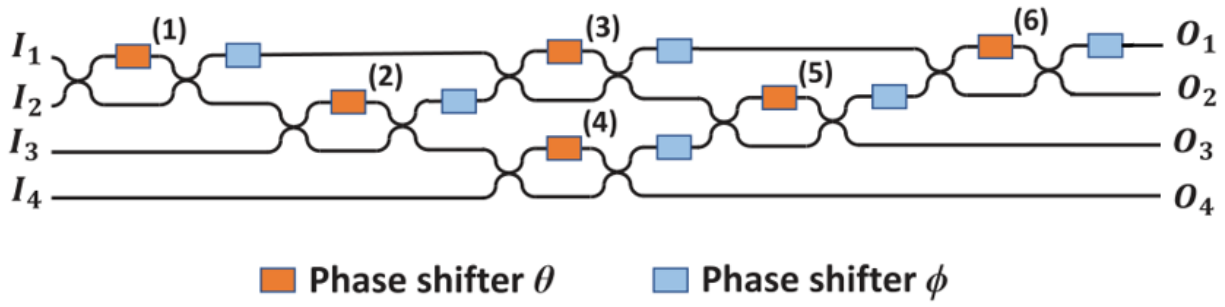

Figure 1.1: 4×4 MZI-based reconfigurable optical processor based on the Reck topology (adopted from [3]) © by F. Shokraneh, used under CC BY 4.0.

$$\begin{bmatrix} O1 \\ O2 \\ O3 \\ O4 \end{bmatrix} = \begin{bmatrix} \\ \text{4x4 MZI-based linear} \\ \text{transformation matrix} \\ \\ \end{bmatrix} \begin{bmatrix} I1 \\ I2 \\ I3 \\ I4 \end{bmatrix} \tag{1.1}$$

Through manipulation of phase shifters in each MZI, the light intensity passing through them is modified. This modification allows for the encoding of specific transformation matrices in the ROP [3].

The performance of ROPs is affected by fabrication process variations, particularly concerning the phase shifters and directional couplers (DCs) within the MZIs. Reported simulation work found that a 2% error in DC splitters and phase shifters lead to an accuracy reduction to 50% from 98% for MNIST image classification tasks [7].

This thesis explores the design of MZI-based ROPs for generating transformation matrices and examines the impact of inaccuracies in DC splitters on ROP performance. This motivates

the design of a single-mode tunable directional coupler that exclusively couples and tunes the fundamental transverse electrical optical mode (TE0). Additionally, we present a mode-selective tunable directional coupler that offers the novelty of selectively tuning and coupling the first-order transverse electrical optical mode (TE1) while bypassing the fundamental TE0 mode entirely. This innovation can be used for scaling ROPs through optical modes, representing a new application of multi-transverse mode MZI-based optical processors [8]. The growing interest in integrating higher-order optical modes into ROPs necessitates mode-selective building blocks. One example is the development of devices that monitor external ϕ phase changes in MZIs within ROPs, which affect the TE0 mode by observing variations in the optical power of the TE1 mode [9].

1.2 SiPh for Mode Division Multiplexing

Mode-division multiplexing (MDM) is a promising technology that harnesses different spatial modes or mode groups within a fiber to carry distinct signal channels to alleviate the constrained transmission capacity of a single-mode fiber (SMF) [10]. The increased data transmission capacity through a single-mode fiber can be done through the integration of diverse multiplexing technologies, including time division multiplexing (TDM) [11], wavelength division multiplexing (WDM) [12], and digital coherent technologies [13]. However, as the capacity of commercial transport systems continues to escalate, the constraints imposed by the maximum input power and the nonlinear Shannon limits result

in an anticipated capacity limit of a few hundred terabits per second for SMFs [14].

To overcome this limitation, data can be transmitted over different optical modes that are (de)multiplexed through mode-division multiplexing (MDM) on-chip systems to then be transmitted onto a few-mode fiber (FMF). This approach involves developing active and passive on-chip MDM devices capable of dynamically combining or separating modes. Recent efforts have focused on exploring methods such as (de)multiplexing the TE modes by coupling with a multi-core bus waveguide [15] or using a tapered directional coupler [16]. Other efforts have focused on extending FMF transmission link lengths without amplifiers to send and receive MDM signals, reaching up to 100 km [17]. Our research team has developed several building blocks for on-chip MDM, as proposed here [18].

This thesis introduces the design of a mode-selective tunable directional coupler (MS-TDC) which serves as a building block within on-chip MDM systems. This device is used for TE0/TE1 mode (de)multiplexing and offers tunability to correct errors and variations resulting from fabrication, thus overcoming the limitations of other designs with its tunability feature.

1.3 Motivations

Within the realm of ROPs, challenges emerge including in the directional couplers used as 50:50 splitters within MZIs. These challenges stem from fabrication errors that affects the overall performance of ROPs. Addressing these fabrication errors is vital for realizing

the full potential of optical processors. Various design strategies have been explored to rectify imperfections in optical beam splitters for ROPs. These strategies include multimode interference (MMI) [19], dual Mach-Zehnder interferometers (DMZI) [20], and hardware error correction through calibration methods [21]. The MMI approach reduces the impact of fabrication errors on overall performance due to its larger footprint, which also simplifies the fabrication process and minimizes the likelihood of errors [19]. However, the larger footprint of MMI is not ideal for designs with chip area constraints due to the need of multiple devices. The DMZI technique involves adding two cascaded MZIs before and after the main MZI. These additional MZIs act as compensators for errors in the beam splitters of the main MZI by adjusting their phases [20]. The integration of these additional components increases both complexity and design size. Hardware error correction through calibration methods involves intricate steps to correct phases and beam splitter errors in MZIs [21]. While promising, this approach remains largely theoretical and lacks practical implementation. In contrast, our simple and straightforward tunable directional couplers (TDC) design has distinctive advantages, offering tunability of the splitting ratio up to 10% addressing challenges related to splitter imperfections at the cost of power dissipation from the heater.

Directional couplers also have applicability in on-chip MDM to (de)multiplexer or combine/separate modes on silicon-on-insulator (SOI) technology platforms. Examples include (de)multiplexing of two transverse electric (TE) modes, the fundamental mode (TE0) and the first-order mode (TE1), using tapered directional couplers [22]. In this

setup, TE0 is injected into both coupler input ports. In the narrower waveguide, the TE0 mode converts to TE1 mode, while in the wider waveguide, the injected TE0 mode remains in the same mode. An asymmetric directional coupler structure can also be employed to split the TE0 and TE1 modes without altering their mode orders [23]. Alternatively, a polarization beam splitter (PBS) can be used within an asymmetrical DC [24]. This configuration separates TE0 and the fundamental transverse magnetic mode (TM0) modes into different output ports, when both modes are emitted from a single input port. Our design of a mode-selective tunable directional coupler (MS-TDC) outperforms these alternatives in several aspects. Unlike other designs, the MS-TDC does not involve mode order conversion during coupling, features symmetric arms, and offers tunability to compensate for fabrication variations. They serve as both (de)multiplexers and combiner/separators for TE0 and TE1 modes, providing enhanced versatility and functionality. The comparison of these MDM directional couplers is summarized in Table 1.1.

Table 1.1: Comparison of directional couplers for MDM systems.

MDM Device	**Mode Order Conversion (Y/N?)**	**Optical Modes**	**Compensation for Fabrication Errors**
Tapered DC [22]	Y	TE0/TE1	No Tunability
Asymmetric DC [23]	N	TE0/TE1	No Tunability
PBS [24]	N	TE0/TM0	No Tunability
MS-TDC	N	TE0/TE1	Tunability

1.4 Thesis Contributions

The research within this thesis spans from conceptualization and design to experimentation and has been undertaken by the MSc student candidate, Hasan Hoji, under the supervision of Prof. Odile Liboiron-Ladouceur. The content comprising this thesis is being considered for publication in a peer-reviewed journal. The primary contributions of this thesis, are elaborated upon below.

The conception, creation, and empirical validation of two distinct designs to introduce tunability in directional couplers: the single-mode TDC, exclusively coupling TE0 mode, and the mode-selective TDC which selectively couples TE1 mode at variable coupling ratios while bypassing the TE0 mode through the through port. Both designs of tunable directional couplers serve multiple critical purposes within optical systems. Primarily, they tackle the performance reduction issue in reconfigurable optical processors (ROPs) by mitigating the adverse effects of fabrication errors. Tunability is introduced in directional couplers, allowing the effective compensation of splitting percentage errors. This is achieved by utilizing the thermal-optic effect through heaters positioned above these couplers. Additionally, MS-TDCs have applications in mode-division multiplexing (MDM) systems, where the on-chip combination or separation of specific optical modes, such as TE0 and TE1 modes. MS-TDCs designed for MDM on-chip systems are engineered to route the TE0 mode to the through port of the coupler output, while directing the TE1 mode to the cross port of the coupler. The tunability inherent in MS-TDCs enables the correction of TE1 splitting percentage

errors, which are more susceptible to fabrication errors due to being less confined within the waveguide.

1.5 Thesis Organization

This thesis comprises five chapters. This initial chapter serves as an introduction, providing a brief overview of ROPs and MDM, followed by a discussion on the motivation, contributions, and organization of the thesis.

The literature review is discussed in Chapter 2 with the theoretical background covering the effects of geometry and thermo-optic properties in waveguide modes, as well as an investigation of the thermal properties of heaters. This chapter also explores directional couplers using the supermode approach and discusses MZIs as building blocks for ROPs, focusing on transformation matrices of MZI meshes for various ROP topologies.

Chapters 3 and 4 are dedicated to the discussion of the two specific coupler designs: the single-mode tunable directional coupler (SM-TDC) and the mode-selective tunable directional coupler (MS-TDC), respectively. Each chapter begins with a detailed examination of the design principles, followed by simulation results, and concludes with experimental findings to validate the simulations. At the end of Chapter 4, future plans for extending the scope of this thesis by introducing other types of MS-TDCs are discussed. These enhancements aim to improve the versatility and functionality of ROPs in multi-mode scenarios.

Finally, Chapter 5 presents the conclusion of the thesis, summarizing key findings from both theoretical studies and experimental validations, and discussion of future work.

Chapter 2

Background

2.1 Optical Waveguides in Silicon-on-Insulator

An optical waveguide is a structural element within photonic integrated circuits, composed of bulk silicon (Si) enveloped by silicon dioxide (SiO_2) in the case of silicon-on-insulator (SOI) technology. Si waveguides have evolved into components that can manipulate passively and actively. These devices, such as directional couplers (DCs), Y-branches, and Mach-Zehnder interferometers (MZIs), leverage the behavior of light within waveguide structures for specific functions.

In the realm of photonic integrated circuits, silicon-on-insulator (SOI) technology stands out for its seamless integration with standard complementary metal-oxide-semiconductor (CMOS) processes, enabling its fabrication with existing foundry infrastructure [25].

SOI has many advantages that make it suitable for different applications in photonics. One of the key benefits is the high index contrast between the Si waveguide and SiO_2 cladding. This high index contrast enables the implementation of unique functionalities within a compact footprint [26]. Additionally, SOI exhibits high temperature sensitivity at a wavelength of 1550 nm, with a thermo-optic coefficient for Si is 1.8×10^{-4} K^{-1} [27]. These characteristics make SOI technology particularly suitable for applications such as modulators and switches [28, 29], including our tunable directional coupler designs.

2.1.1 Fabrication Process

The devices presented in this thesis were fabricated using silicon-on-insulator (SOI) technology provided by Applied Nanotools (ANT) [30]. The SOI wafer consists of three layers: a 725 µm thick silicon handle layer, a 2 µm SiO_2 buried oxide layer, and a 220 nm thick silicon device layer. The fabrication process begins with cleaning the wafer, followed by spin-coating a material called resist onto the silicon device layer. This resist is sensitive to electron beam exposure.

Using 100 keV electron beam lithography (EBL), a focused beam of electrons is directed onto the resist layer in a specific pattern corresponding to the desired device layout, achieving a minimum feature size of 60 nm and a minimum spacing of 70 nm. After the electron beam exposure, the resist is chemically developed to reveal the pattern. Subsequently, an anisotropic inductively-coupled-plasma reactive ion etching (ICP-RIE)

process is used to transfer this pattern into the silicon layer. The etching continues until the silicon is completely removed, exposing the underlying oxide layer.

Once the silicon devices and waveguides are accurately patterned, a 2.2 µm SiO_2 cladding layer is deposited via plasma-enhanced chemical vapor deposition (PECVD) to protect and electrically isolate the photonic devices from the external environment. In parallel, a tri-layer metallization process is performed to fabricate active metal heaters made from titanium tungsten (TiW), used for thermal tuning.

Finally, an additional 300 nm layer of SiO_2 is deposited as passivation to protect the heaters from oxidation. The total SiO_2 cladding thickness amounts to 2.5 µm. A schematic of the fabrication process is shown in Figure 2.1.

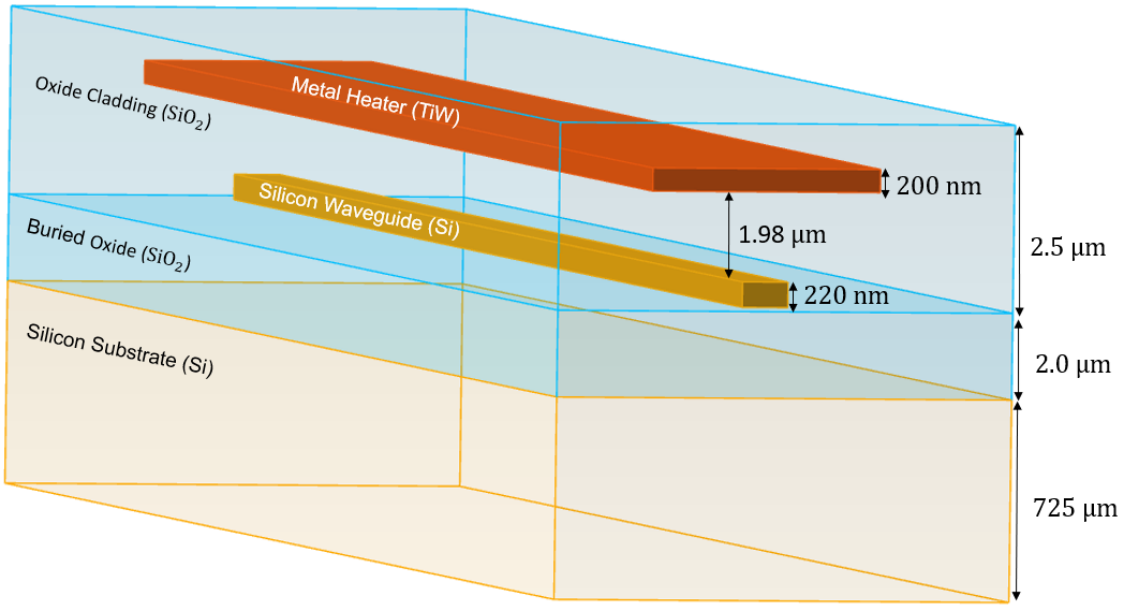

Figure 2.1: Schematic diagram illustrating the cross-sectional dimensions of ANT photonics chips (dimensions not to scale).

2.1.2 Waveguide Optical Modes

Understanding the behavior of transverse electric optical (TE) modes within strip waveguides comprising a rectangular Si layer with a thickness of 220 nm surrounded by SiO_2 is crucial for the designs presented in this thesis. Given that the waveguide thickness remains fixed at 220 nm, as dictated by the SOI technology at ANT, the width of the waveguide becomes the adjustable parameter. In Figure 2.2, the effective indices of the waveguide modes are depicted in relation to the width of a strip waveguide. At a width of 440 nm, the TE1 mode effective refractive index equals the refractive index of SiO_2, which is 1.42 [31]. At this width, TE1 mode starts to be guided in the waveguide.

In the design of the single-mode TDC, a width of 500 nm is chosen. This choice is driven by the fact that the single-mode TDC design is specifically tailored for the fundamental transverse electrical optical mode (TE0) coupling. Conversely, for the mode-selective TDC, a width of 800 nm is selected. This wider width accommodates the TE0 mode, the first-order transverse electric optical mode (TE1), and the fundamental transverse magnetic mode (TM0). This thesis focuses on studying the manipulation and coupling of the TE0 and TE1 electrical optical modes using the mode-selective TDC.

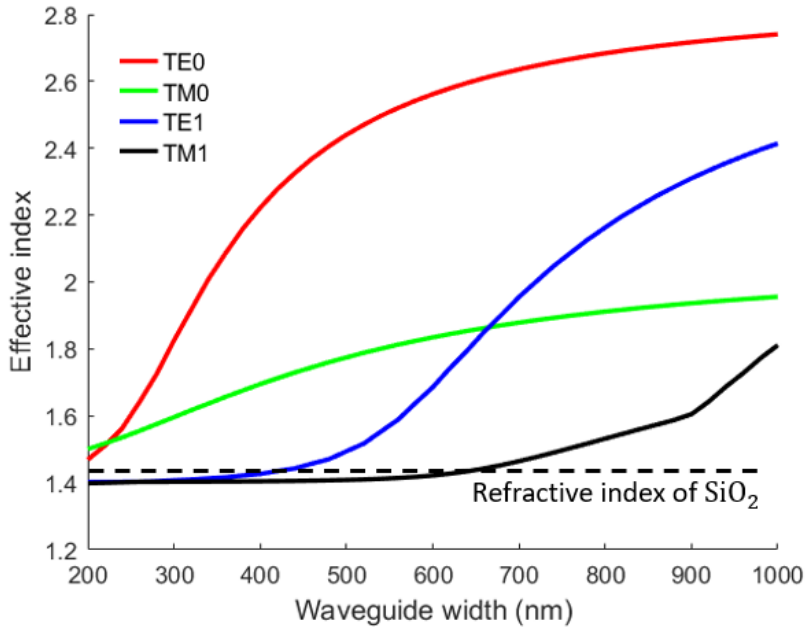

Figure 2.2: Simulation conducted in Ansys/Lumerical MODE of the effective index of the waveguide modes versus the width of a strip waveguide with a height of 220 nm, performed at a wavelength of 1550 nm. The horizontal dashed line represents the refractive index for the waveguide cladding (SiO_2).

2.2 Tuning Using Heaters

2.2.1 Thermo-optic Effect

The single-mode TDC and mode-selective TDC designs discussed in this thesis utilize a titanium tungsten (TiW) metal heater positioned above the waveguides. This configuration induces temperature changes (ΔT) in the waveguides, leading to changes in the material's refractive index (Δn), a phenomenon referred as the thermo-optic effect. The thermo-optic coefficient (TOC) for silicon at a wavelength of 1550 nm has been experimentally determined

to be $TOC = \frac{\Delta n}{\Delta T} = 1.8 \times 10^{-4}$ K^{-1} [27]. Figure 2.3 plots the Sellmeier equation for silicon [32], illustrating the relationship between refractive index change and wavelength, known as dispersion, at different temperatures for wavelengths ranging from 1400 nm to 1600 nm. The plot reveals that for small wavelength ranges, such as 50 nm, there is a linear relationship between refractive index changes (Δn) and wavelength changes ($\Delta \lambda$). Consequently, at a given refractive index (n), a linear relationship can be established between changes in wavelength and temperature changes, as expressed in following equation:

$$\Delta \lambda = \lambda \frac{\Delta n}{n} = \frac{\lambda \cdot \Delta T \cdot TOC}{n} \tag{2.1}$$

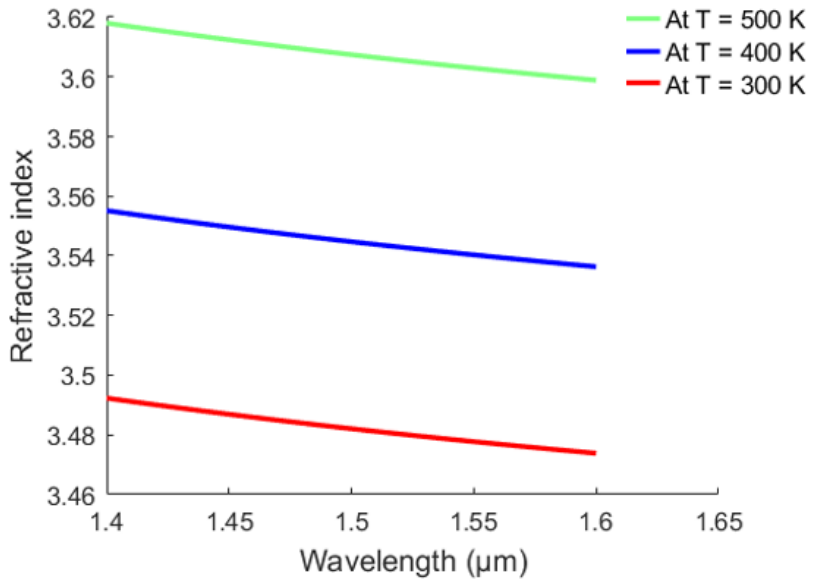

Figure 2.3: Change in the refractive index with wavelengths for silicon at different temperatures using Sellmeier equation.

2.2.2 Titanium Tungsten Thermal Properties

Our designs are fabricated at the Applied Nanotools (ANT) foundry, where a TiW alloy serves as the metal heater material. This alloy comprises 10% titanium (Ti) and 90% tungsten (W). It is deposited with a thickness of 200 nm and is positioned at a distance of 1.98 µm above the waveguides [30] (see Figure 2.1).

The thermal properties of the TiW alloy are important, particularly because they are necessary to configure heat-related simulation softwares such as the Ansys/Lumerical HEAT solver. This setup enables accurate modeling of heaters. These properties include:

- **Metal Density**: The density (D) of the TiW alloy, approximately 14,523 kg/m^3, is calculated based on the individual densities of titanium (Ti) and tungsten (W), which are 4,500 kg/m^3 and 19,300 kg/m^3, respectively [32]. Taking into account their respective weight percentages in the TiW alloy, the metal density is calculated with the equation below [33]:

$$\frac{1}{D_{\text{TiW}}} = \frac{0.1}{D_{\text{Ti}}} + \frac{0.9}{D_{\text{W}}} = \frac{0.1}{4,500} + \frac{0.9}{19,300} = \frac{5980}{86.85 \times 10^6}, \quad D_{\text{TiW}} \approx 14,523 \text{ kg/m}^3 \quad (2.2)$$

  Density plays a crucial role in determining the mass of a material per unit volume. In thermal simulations, the density of the material directly impacts its capacity to store heat and its response to temperature variations. Equation 2.3 represents the heat exchange equation, illustrating the heat supplied to or consumed by the surrounding

environment of the metal as expressed in following equation [33]:

$$Q_h = c \times m \times \Delta T \tag{2.3}$$

where Q_h represents the heat supplied to the system in units of joules (J), m denotes the mass of the system in units of kilograms (kg), which is equal to the density multiplied by the volume of the heater derived from its geometry, c is the heat capacity of the system in units of joules per kilograms-kelvin (J/kg $\cdot$ K) that we discuss following, and ΔT represents the change in temperature of the system in units of kelvin (K).

- **Heat Capacity**: This is a material-specific constant representing the amount of heat per unit mass required to raise the temperature of the material by one kelvin degree. In simulation, the importance of the heat capacity c of the TiW heater lies in determining the amount of heat supplied by conduction to the silicon device under study, specifically in this work the tunable directional coupler (Eq. 2.3). Unfortunately, the heat capacity of TiW is not readily available. However, it can be estimated to be equal to the heat capacity of pure tungsten, which is approximately 132.0 J/kg·K [32] once it contribute 90% of the alloy.

- **Electrical Conductivity**: It is a measure of the ability of the material to conduct an electrical current. In heat-related simulations, electrical conductivity is important for modeling Joule heating and calculating the thermal conductivity. The electrical

conductivity (σ) of the TiW alloy is the reciprocal of its bulk resistivity, which is approximately $0.61 \times 10^{-6}\ \Omega \cdot \mathrm{m}$ [30]. This translates to an electrical conductivity of roughly 1.64×10^{6} S/m.

- **Thermal Conductivity**: Thermal conductivity quantifies a material's ability to conduct heat, essential for accurately modeling heat transfer processes such as conduction, convection, and radiation, and for relating these processes to the power dissipated in the material. Estimating the thermal conductivity (κ) of TiW involves using the Wiedemann-Franz law [34], which relates thermal conductivity to electrical conductivity. At room temperature (T), 298 K, the Lorenz number (L_o) is approximately $2.45 \times 10^{-8}\ \mathrm{W{\cdot}\Omega{\cdot}K^{-2}}$. Using this formula, we find the thermal conductivity of TiW is approximately 12.0 W/m·K, as follows:

$$\kappa = \sigma L_o T = 1.64 \times 10^{6} \times 2.45 \times 10^{-8} \times 298 \approx 12.0\ \ \mathrm{W/m{\cdot}K} \tag{2.4}$$

2.2.3 Metal Heater Resistivity

Designing metal heaters involves selecting the appropriate dimensions, directly influencing their resistivity. Calculating the resistivity of metal heaters is crucial since it enables the measurement of the dissipated electrical power in the metal. Electrical power is used as a metric for comparing and calculating the efficiency of the devices. This is achieved by multiplying the resistivity of the metal by the square of the current flowing through it.

Integrated photonics foundries, such as ANT, commonly specify sheet resistance in units of ohms per square ($\Omega/\square$). The reported value for TiW metal heater is 3.04 $\Omega/\square$. This information determines the resistance of the heater through the following formula:

$$R = \frac{Rs \cdot L}{W} \tag{2.5}$$

where R is the resistance of the metal in ohms, R_s is the sheet resistance, L is the length of the heater, and W is the width of the metal heater.

2.2.4 Power Dissipation in Metal Heater

In section 2.2.1 entitled thermo-optic effect, the relationship between the temperature change (ΔT) in silicon waveguides and the resulting wavelength shift ($\Delta\lambda$) is derived. Despite the significance of this equation, its practical application remains challenging due to the difficulty of directly measuring temperature changes in silicon during operational processes. Many research studies in silicon photonics opt for an alternative approach, focusing on quantifying the power dissipated in the heater [35, 36]. This approach proves more feasible and practical for thermal analysis.

A linear relationship emerges between the applied electrical power to the metal heater and the resulting temperature change within the silicon waveguide, as shown in simulations using the Ansys/Lumerical HEAT solver depicted in Figure 2.4. These findings lead to the

conclusion that a linear relationship exists between the applied electrical power (P) to the metal heater and the wavelength shift ($\Delta\lambda$) in silicon waveguides.

When current flows through the metal heater, it increases the temperature, which can eventually lead to failure due to melting. In Chapter 3, we will discuss in detail the maximum allowable current and power that can be applied to the heater before failure occurs. However, both simulations and experiments show that the temperature of the coupling waveguides increases by around 350 K before metal failure, as indicated by the horizontal green dashed line (Fig. 2.4), regardless of the heater dimensions.

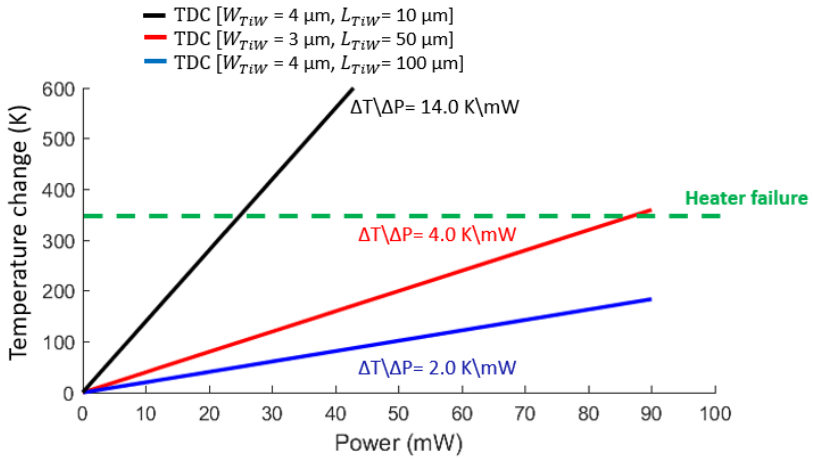

Figure 2.4: Change in temperature relative to 300 K of the coupling waveguides as a function of applied electrical power (P) for a 6 µm coupling length in a SM-TDC, considering different combinations of heater widths (W_{TiW}) and lengths (L_{TiW}). The horizontal dashed line represents the temperature rise of the coupling waveguides at metal failure.

2.3 Directional Couplers

Directional couplers are essential elements in integrated photonics, facilitating the efficient transfer of optical power between two adjacent waveguides. This occurs through coupling when the evanescent field from one waveguide extends into the core of the neighboring waveguide [37].

These components hold a pivotal role across diverse photonic applications, spanning from wavelength division multiplexing (WDM) systems, where multiple data streams are transmitted simultaneously using different wavelengths of light [38], to the development of ROPs [3], instrumental in performing matrix multiplications within computational systems such as optical neural networks. Furthermore, directional couplers find relevance in emerging technologies such as mode division multiplexing (MDM) [39], which uses distinct spatial modes within optical fibers to increase data transmission.

In the following sections, we will explore the theoretical foundations and design factors pertaining to directional couplers. These components serve as foundational elements for the single-mode TDCs and mode-selective TDCs discussed in this thesis.

2.3.1 Supermode Theory Approach

The supermode approach, also known as the Eigenmode Expansion Method [40], is a sufficiently accurate technique for simulating electromagnetic wave propagation in uniform waveguides. In directional couplers, this method involves calculating the coupling

coefficient for each waveguide by determining the two eigenmodes for each optical mode: the symmetric and asymmetric supermodes, which coexist simultaneously in both coupler waveguides [41].

Eigenmodes are characteristic solutions to Maxwell's equations within the waveguide cross-section. The eigenvalues represent the propagation constants of these electromagnetic waves. The eigenvectors describe the field distributions of the electromagnetic waves within the waveguides. Thus, the eigenmodes (supermodes) capture the periodic behavior of the propagating modes [42, 43]. The process of calculating the coupling coefficient using the supermodes approach will be elaborated in this section.

In Figure 2.5, the fundamental transverse electrical optical (TE0) mode is injected into waveguide 1. The two straight parallel strip waveguides have a strip cross-section of 500×220 nm^2 separated by a 200 nm gap, resulting in the simultaneous excitation of two supermodes in each waveguide.

Figure 2.6 (a,c) illustrates the E_y fields for the symmetric supermode, where the electric field in both waveguides 1 and 2 are in phase. Conversely, Figure 2.6 (b,d) shows the asymmetric supermode, where there is a π phase difference between waveguides 1 and 2. Figure 2.6 (e,f) shows the resultant TE0 mode, which is the vectorial summation of these simultaneous supermodes [41]. As light propagates through the waveguide, the phase of the two supermodes changes, following the sinusoidal behavior of the propagating electromagnetic wave in the waveguide. This phase variation causes the field intensity to

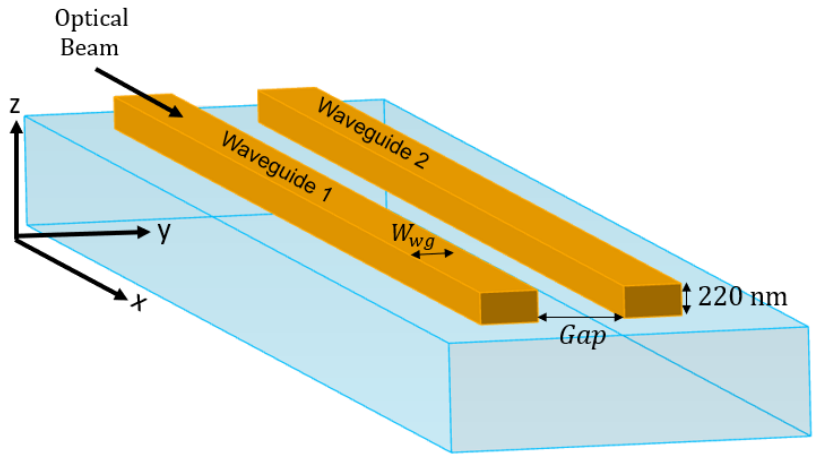

Figure 2.5: Schematic of a coupler with two straight parallel strip waveguides, with the direction of the injected optical signal indicated. The waveguide width (W_{wg}) is 500 nm for single-mode TDC and 800 nm for mode-selective TDC (dimensions not to scale).

oscillate between the two waveguides. Each supermode is characterized by an effective refractive index (n_{eff}) and a propagation constant (β). The propagation constant of each supermode is expressed as follows:

$$\beta_1 = \frac{2\pi.n_{eff1}}{\lambda} \text{ for symmetric supermode} \tag{2.6}$$

$$\beta_2 = \frac{2\pi.n_{eff2}}{\lambda} \text{ for asymmetric supermode} \tag{2.7}$$

The propagation constant of the symmetric supermode (β_1) is slightly greater than that of the asymmetric supermode (β_2). This is because the constructive interference between the symmetric fields in the two waveguides leads to greater confinement and thus a higher propagation constant. Conversely, the destructive interference between the fields in the two

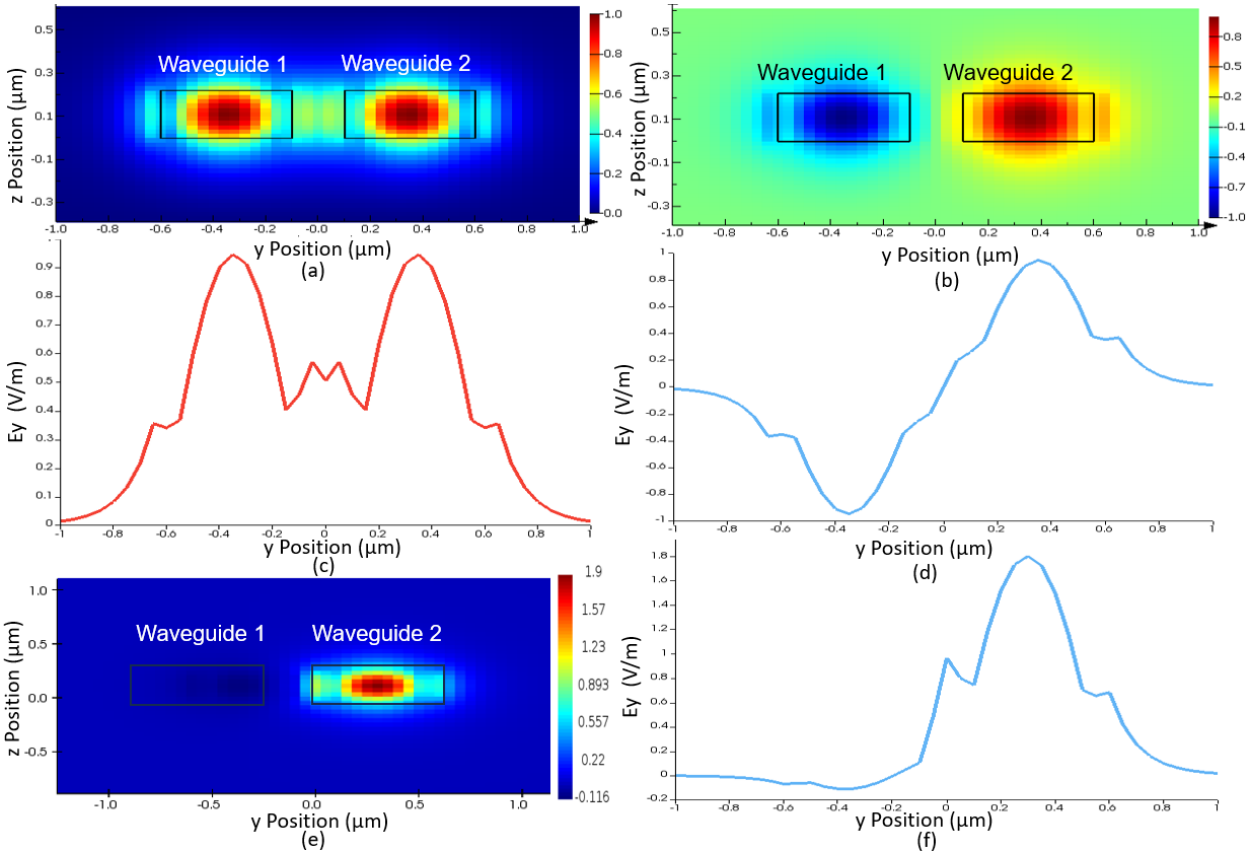

Figure 2.6: Electric field intensity distribution (E_y) for the TE0 mode and its supermodes for a directional coupler: real part for (a) the symmetric supermode and (b) the asymmetric supermode, cross-section of the real part along the z-axis for (c) the symmetric supermode and (d) the asymmetric supermode, (e) real part for the resultant TE0 mode obtained by vectorial summation of the symmetric and symmetric modes, (f) cross-section of the real part along the z-axis for the resultant TE0 mode in (e).

waveguides in the asymmetric mode leads to weaker confinement and a lower propagation constant [44]. To increase or decrease the difference in the effective refractive indices, and thus the difference in propagation constants for these supermodes, we can adjust parameters such as the waveguide separation (gap), waveguide width, the operating

wavelength, or the waveguide temperature. Decreasing the gap increases the difference as it enhances the constructive and destructive interference between the symmetric and asymmetric fields, respectively. This enhancement leads to a higher propagation constant for the symmetric supermode and a lower one for the asymmetric supermode. This difference is key to calculating the mode coupling coefficient, as follows [45]:

$$C = \frac{\beta_1 - \beta_2}{2} = \frac{\pi \Delta n_{eff}}{\lambda} \tag{2.8}$$

Subsequently, the optical coupling power flow over the coupling length (L) can be expressed as [40]:

$$\cos^2(C \cdot L) = \cos^2\left(\frac{\pi \Delta n_{eff} \cdot L}{\lambda}\right) \text{ in waveguide 1} \tag{2.9}$$

$$\sin^2(C \cdot L) = \sin^2\left(\frac{\pi \Delta n_{eff} \cdot L}{\lambda}\right) \text{ in waveguide 2} \tag{2.10}$$

Equations (2.9) and (2.10) define the optical power transfer between the coupling waveguides, which depends on both the coupling waveguide length (L) and the mode coupling coefficient (C). Changing either of these parameters will impact the optical power transfer in a sinusoidal pattern since they both appear within the sinusoidal function. The crossover length (L_x), where optical power is completely transferred from waveguide 1 to

waveguide 2, can be derived as follows:

$$\sin^2\left(\frac{\pi\Delta n_{eff}L_x}{\lambda}\right) = 1 = \sin^2\left(\frac{\pi}{2}\right), \tag{2.11}$$

which simplifies to

$$L_x = \frac{\lambda}{2\Delta n_{eff}}. \tag{2.12}$$

Similar to the fundamental mode (TE0), the TE1 mode exhibits two distinct supermodes: the symmetric and asymmetric supermodes, each with their respective effective refractive index, denoted as n_{eff3} and n_{eff4}, respectively. Equations (Eq. 2.9) and (Eq. 2.10) are also applied in this context, with Δn_{eff} representing the difference between n_{eff3} and n_{eff4} in the core of TE1.

Figure 2.7 illustrates the E_y field for both symmetric and asymmetric supermodes and the resultant TE1 mode, which is the vectorial summation of both symmetric and asymmetric supermodes, where the TE1 mode is injected into waveguide 1 and the waveguides have a cross-section of 800 $\times$220 nm^2 and are separated by a 200 nm gap (Fig. 2.5).

In this thesis, the single-mode TDC and the mode-selective TDC will be further investigated through both simulations and experimental results using the theory discussed.

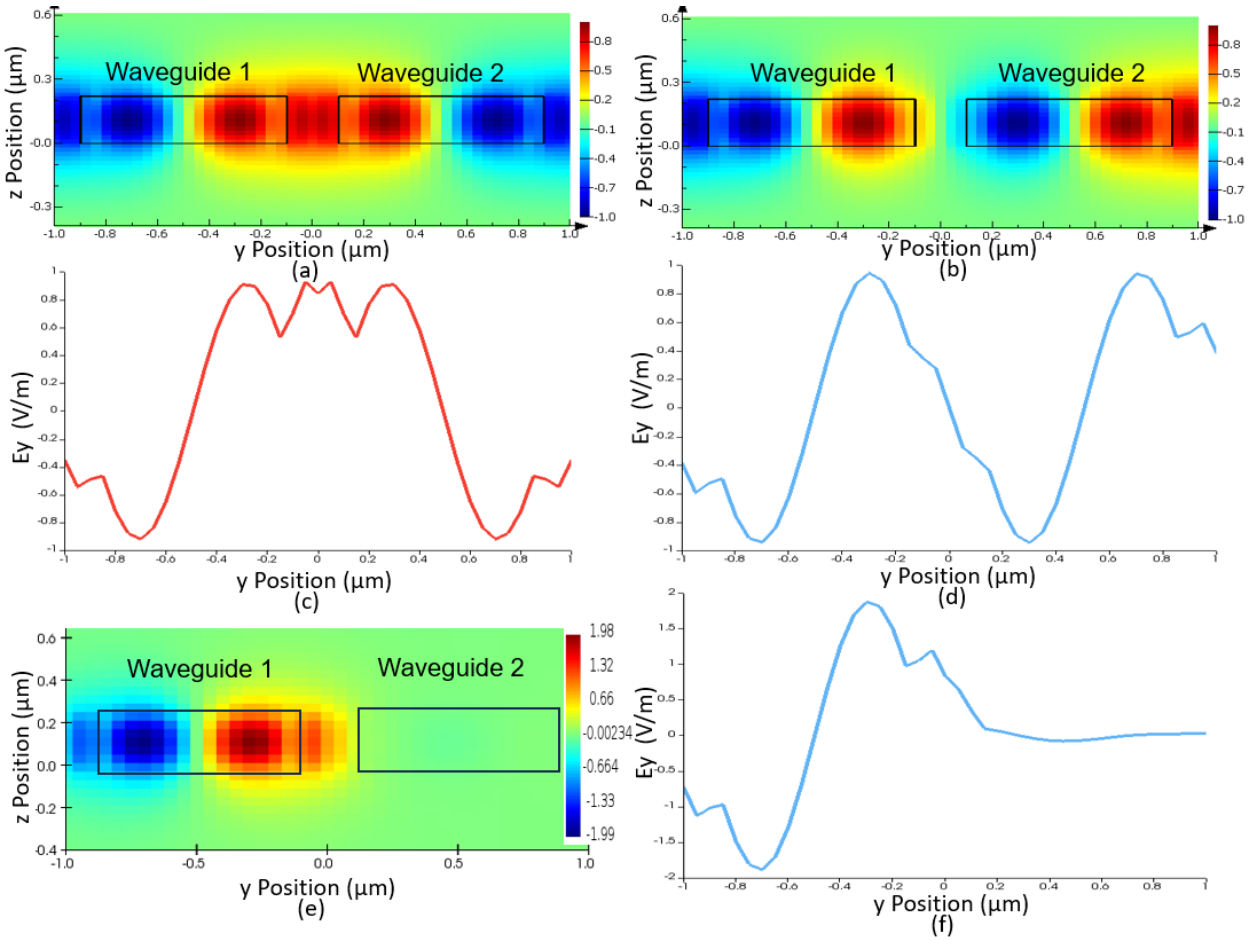

Figure 2.7: Electric field intensity distribution (E_y) for TE1 mode and its supermodes of a directional coupler: real part for (a) the symmetric supermode and (b) the asymmetric supermode, cross-section of the real part along the z-axis for (c) the symmetric supermode and (d) the asymmetric supermode, (e) real part for the resultant TE1 mode obtained by vectorial summation of the symmetric and symmetric modes, (f) cross-section of the real part along the z-axis for the resultant TE1 mode in (e).

2.3.2 Impact of the Coupler Gap Separation

The coupler gap representing the separation distance between the two waveguides in the directional coupler (DC) plays a crucial role in the design and performance of the DC. A

smaller gap results in a stronger overlap of the evanescent electric field between the two coupling waveguides, leading to better coupling and shorter waveguide coupling lengths. Conversely, a larger gap weakens the coupling due to weaker evanescent field overlap, requiring longer coupling lengths [37]. The gap separation also directly influences the difference in the effective refractive indices of the coupler supermodes, which in turn affects the coupling coefficient, as discussed in the previous section. Therefore, the coupler gap parameter significantly influences mode coupling, especially in designing MS-TDCs.

In this thesis, the MS-TDC is examined using 800 nm wide waveguides. These waveguides exhibit the ability to support both TE0, TE1, and the fundamental transverse magnetic (TM0) modes (Fig. 2.2). However, our research focuses on the TE0 and TE1 modes, allowing for the selective coupling of the TE1 mode through different coupling ratios by applying heat. Simultaneously, the TE1 mode is less confined and has a stronger evanescent field overlap in the gap, making it easier to couple in shorter waveguide coupling lengths for the same coupler gap, as illustrated in Figure 2.8, while TE0 remains uncoupled. The crossover length, where optical power is entirely transferred to the cross waveguide, is approximately 19 µm for the TE1 mode and 200 µm for the TE0 mode, given a coupler gap of 200 nm. This difference confirms that the coupling of TE1 is more sensitive to thermal change, while TE0 is not.

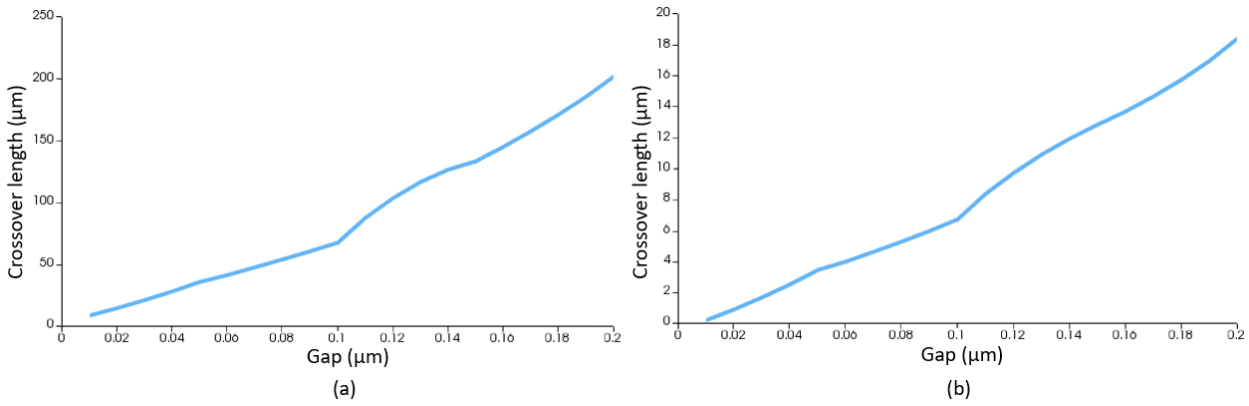

Figure 2.8: Optical transmission crossover length versus coupler gap at 1550 nm and 800×220 nm^2 waveguides: (a) TE0 mode and (b) TE1 mode.

2.4 Mach-Zehnder Interferometer

The Mach-Zehnder interferometer (MZI) plays a pivotal role in numerous optical applications, serving as an essential component in modulators, switches, sensors, and optical processors. Optical processors are the primary focus of this thesis. Illustrated in Figure 2.9 is an MZI as a building block in ROPs constituting of a 2×2 structure comprising two directional couplers (also referred as beamsplitters) and two phase shifters, θ and ϕ.

The optical output power of the MZI is directly influenced by the θ phase, as adjustments to this phase introduce a phase difference between the upper and lower arms of the MZI. At the MZI output, this phase difference varies from constructive interference (maximizing output power at output port 1) when waves are in phase to destructive interference (minimizing output power at output port 2) when out of phase by π radians.

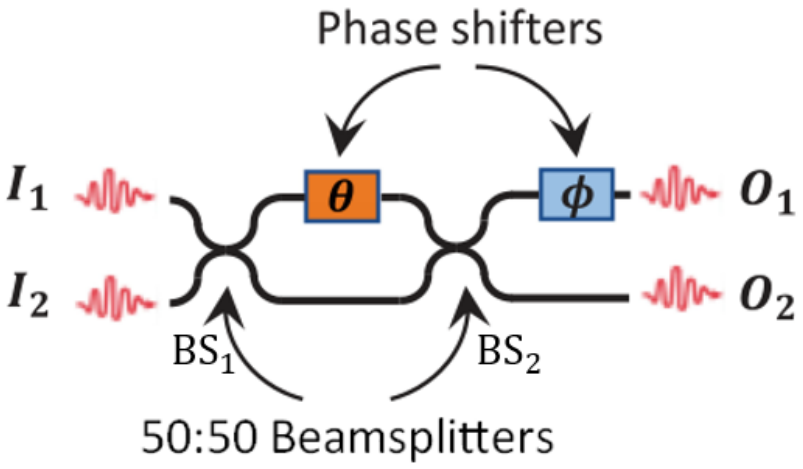

Figure 2.9: A 2×2 MZI building block with phase shifters denoted by θ and ϕ, (adopted from [3]) © by F. Shokraneh, used under CC BY 4.0.

The ϕ phase governs the relative phase difference between the two output ports and is necessary for cascading MZIs in optical processors. Both beamsplitters in the MZI are configured to achieve a 50:50 splitting ratio.

The complete response of the MZI can be illustrated using a unitary transformation matrix, a mathematical representation describing linear transformations that preserve the norm (length) of vectors in a vector space [46]. Unitary transformation matrices preserve the optical power (represented by the length of the vector) during the manipulation of light signals assuming a lossless ROP. Furthermore, unitary transformations maintain the inner product of vectors, which includes both amplitude and phase information such that the phase information of the optical signal is preserved during propagation and manipulation. MZI unitary matrix transformation is defined by multiplying the transformation matrices (R) of its individual components, the two phase shifters (Eq. 2.13) and the two beamsplitters

(Eq. 2.14).

$$R_\theta = \begin{bmatrix} e^{j\theta} & 0 \\ 1 & 0 \end{bmatrix}, R_\phi = \begin{bmatrix} e^{j\phi} & 0 \\ 1 & 0 \end{bmatrix} \tag{2.13}$$

$$R_{BS} = \begin{bmatrix} \sqrt{\rho} & j\sqrt{1-\rho} \\ j\sqrt{1-\rho} & \sqrt{\rho} \end{bmatrix}, \text{if } \rho = 0.5 \text{ then } R_{BS} = \frac{1}{\sqrt{2}} \begin{bmatrix} 1 & j \\ j & 1 \end{bmatrix} \tag{2.14}$$

where ρ is the splitting ratio of the MZI beamsplitters, which is set to 50% assuming no fabrication variation. ρ with fabrication variations will be studied in section 2.4.2. The unitary matrix transformation of an MZI becomes the following expression:

$$R_{MZI} = R_\phi . R_{BS} . R_\theta . R_{BS} = j e^{j(\frac{\theta}{2})} \begin{bmatrix} e^{j\phi} \sin\left(\frac{\theta}{2}\right) & e^{j\phi} \cos\left(\frac{\theta}{2}\right) \\ \cos\left(\frac{\theta}{2}\right) & -\sin\left(\frac{\theta}{2}\right) \end{bmatrix} \tag{2.15}$$

2.4.1 MZIs in Reconfigurable Optical Processors

MZIs play a foundational role in ROPs. Configurations of MZI photonic circuits can physically emulate forward-only computation in neural networks [47], by representing synaptic weight matrices W through optical power transmission matrices T. Fabrication variations observed in directional couplers have been known to cause splitting deviations of approximately ±2% to ±3% in SOI directional couplers [48]. Reported simulation work has shown that a 2% inaccuracy only in DC splitters leads to a reduction to 65% from 98% for MNIST image classification tasks for a 8×8 MZI-based topology [7]. The key result of this

study is shown in Figure 2.10.

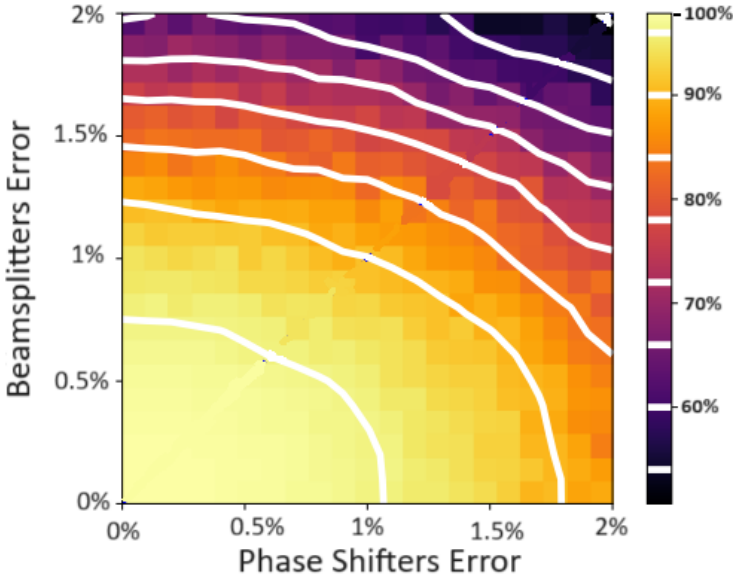

Figure 2.10: MNIST classification accuracy for an 8×8 MZI-based topology as a function of phase shifters error and beamsplitters error (adopted from [7]) © 2019 Optical Society of America under the terms of the OSA Open Access Publishing Agreement.

Different ROP topologies are built based on MZI unitary transformation matrices under ideal conditions with 50:50 beamsplitters ($\rho = 0.5$). Imperfections in beamsplitters affect the MZI transformation matrix differently and subsequently impact their weight matrices. To explore ROP configurations based on MZI arrangements and the impact of imperfect splitters, the Reck [6] and Clements [49] topologies are discussed. These configurations involve triangular and rectangular MZI mesh based topologies respectively, as shown in Figure 2.11 (a,b). The number of MZIs for an $N \times N$ weight matrix W is given by $n = \frac{N(N-1)}{2}$ for both topologies. Manipulating the θ and ϕ phases of each MZI generates the required

weight matrix on the photonic chip. The $N \times N$ weight matrix W is constructed through a product of n diagonal matrices D, where each D matrix is of the same size as the W matrix. The product of the D matrices follows a descending order, starting from D_n down to D_1, as shown in the following equation where order k is determined by the position of the MZI within a given topology.

$$W = \prod_{k=n}^{1} D_k \tag{2.16}$$

Each matrix D linearly relates a specific input optical signal to an output in the photonic topology. This relationship is achieved by adjusting the phases of the related MZI [50], highlighting the importance of understanding the numbering of MZIs for a given ROP topology. Figure 2.11 displays the proper numbering of MZIs in the topologies, corresponding to the numbering of the D matrices. The number in the blue boxes of the MZI starts from the input side on the left and increases from top to bottom for MZIs located in the same vertical layer. After numbering all MZIs in a vertical layer, the numbering continues from left to right across vertical layers. For example, in Figure 2.11(b):

- For the first vertical layer from the input side on the left, there are two MZIs. Numbering starts from top to bottom, with the upper MZI numbered as MZI_1 and the lower MZI as MZI_2.

- For the next vertical layer to the right, there is one MZI, which is numbered as MZI_3.

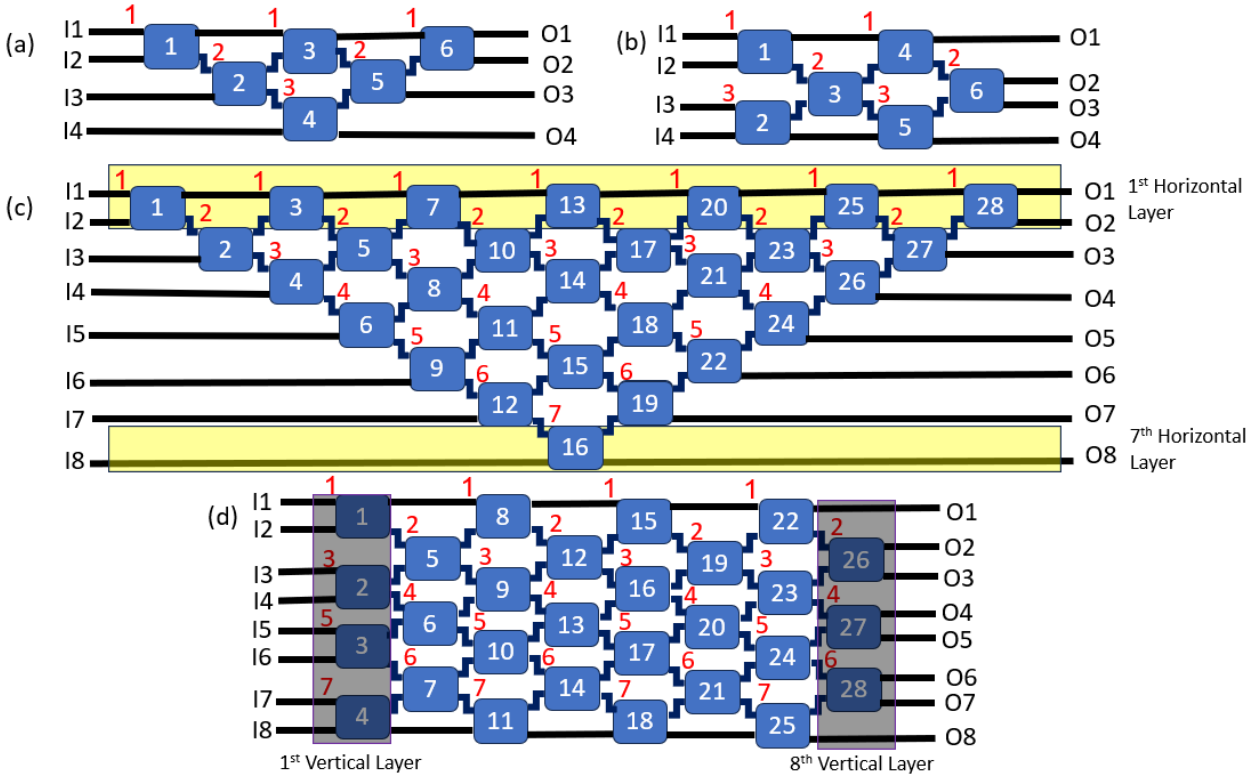

Figure 2.11: Four MZI mesh topologies: (a) 4×4 Reck, (b) 4×4 Clements, (c) 8×8 Reck, (d) 8×8 Clements. Each numbered blue rectangle symbolizes an MZI, and each red number indicates the corresponding index on their diagonal matrix. The yellow and gray rectangles highlight examples of horizontal and vertical layers, respectively.

- The following vertical layer to the right has two MZIs. The upper MZI is numbered as MZI_4 and the lower MZI as MZI_5.

- The last vertical layer to the right has one MZI, which is numbered as MZI_6.

To construct all the D matrices, each 2×2 MZI transformation matrix R_{MZI} (Eq. 2.15) should be inserted into its corresponding $N \times N$ D matrix at specific (row, column) indices. These indices are indicated by the red numbers at the input of each MZI in the topologies

shown in Figure 2.11. The red numbers are distributed such that all MZIs on the same horizontal layer have the same number, starting from the top horizontal layer and increasing down to the last layer. For example, in Figure 2.11(a):

- MZI_1, MZI_3, and MZI_6 lie in the first horizontal layer, indicating that the 2×2 R_{MZI} matrices for them will be inserted at the (1,1) indices in their respective D matrices ($D1$, $D3$, and $D6$).
- MZI_2 and MZI_5 lie in the second horizontal layer, implying that the 2×2 R_{MZI} matrices for them will be inserted at the (2,2) indices in their respective D matrices ($D2$, $D5$).
- MZI_4 lies in the third horizontal layer, implying that the 2×2 R_{MZI} matrix for it will be inserted at the (3,3) indices in its D matrix ($D4$).

The six D matrices (i.e., D_1 to D_6) for the 4×4 Reck topology can be represented as follows, where R_{MZI} is given in Equation 2.15.

$$D_{1,3,6} = \begin{bmatrix} \begin{bmatrix} & \\ & R_{MZI(1,3,6)} \\ & \end{bmatrix} & 0 & 0 \\ & & 0 & 0 \\ 0 & 0 & 1 & 0 \\ 0 & 0 & 0 & 1 \end{bmatrix}, D_{2,5} = \begin{bmatrix} 1 & 0 & 0 & 0 \\ 0 & \begin{bmatrix} & \\ & R_{MZI(2,5)} \\ & \end{bmatrix} & 0 \\ 0 & & 0 \\ 0 & 0 & 0 & 1 \end{bmatrix}, D_4 = \begin{bmatrix} 1 & 0 & 0 & 0 \\ 0 & 1 & 0 & 0 \\ 0 & 0 & \begin{bmatrix} & \\ & R_{MZI(4)} \\ & \end{bmatrix} \\ 0 & 0 & \end{bmatrix} \tag{2.17}$$

2.4.2 Impact of Imperfect MZI Splitters on ROPs

To delve into the effect of imperfections in DC splitters on MZI meshes that compose ROPs, we will start by deriving the unitary matrix transformation of a single MZI with incorporated uncertainties in the DC splitters. Assuming imperfect power splitting ratios α and β for beamsplitters of BS_1 and BS_2, respectively (Fig. 2.9) the transformation matrix R_{MZI} becomes the following matrix:

$$\begin{aligned} R_{MZI} &= \begin{bmatrix} e^{j\phi} & 0 \\ 1 & 0 \end{bmatrix} . \begin{bmatrix} \sqrt{\beta} & j\sqrt{1-\beta} \\ j\sqrt{1-\beta} & \sqrt{\beta} \end{bmatrix} . \begin{bmatrix} e^{j\theta} & 0 \\ 1 & 0 \end{bmatrix} . \begin{bmatrix} \sqrt{\alpha} & j\sqrt{1-\alpha} \\ j\sqrt{1-\alpha} & \sqrt{\alpha} \end{bmatrix} \\ &= \begin{bmatrix} \sqrt{\beta\alpha}e^{j(\phi+\theta)} - \sqrt{(1-\beta)(1-\alpha)}e^{j\phi} & j\sqrt{\beta(1-\alpha)}e^{j(\phi+\theta)} + j\sqrt{(1-\beta)\alpha}e^{j\phi} \\ j\sqrt{(1-\beta)\alpha}e^{j\theta} + j\sqrt{\beta(1-\alpha)} & -\sqrt{(1-\beta)(1-\alpha)}e^{j\theta} + \sqrt{\beta\alpha} \end{bmatrix} \end{aligned} \tag{2.18}$$

To quantify the impact of imperfections in DC splitters, we analyze the deviation percentage from the ideal 50:50 splitting ratio in MZIs within a 4×4 triangular Reck topology (Fig. 2.11(a)) . A 2% inaccuracy in the splitters results in a 49:51 splitting ratio. We use the phases listed in Table 2.1, corresponding to a practical example demonstrated experimentally by our group in [3] which used a 4×4 Reck topology (Fig. 2.11(a)).

Table 2.1: Phase value for a practical example for a 4×4 Reck topology (units in radians).

θ_1	θ_2	θ_3	θ_4	θ_5	θ_6
1.7453	1.5708	1.3962	1.2217	1.0472	0.8727
ϕ_1	ϕ_2	ϕ_3	ϕ_4	ϕ_5	ϕ_6
0.0872	0.1745	0.2618	0.3491	0.4363	0.5236

Using phase values, the weight matrix for the ideal 50:50 splitting ratio, W_{ideal}, and the weight matrix for a 2% inaccuracy in the splitting ratio, W_{error}, are given by Equations 2.19 and 2.20, respectively. The calculation of these matrices used the theory discussed earlier by multiplying the diagonal matrices D in descending order. For the ideal 50:50 splitting ratio, R_{MZI} is given by Equation 2.15, and for the 2% inaccuracy in the splitting ratio, R_{MZI} is given by Equation 2.18.

$$W_{ideal} = \begin{bmatrix} (-0.2341 + 0.0030i) & (-0.1011 + 0.1765i) & (0.5216 + 0.4673i) & (0.1664 + 0.6210i) \\ (0.0953 + 0.2949i) & (0.7782 + 0.2674i) & (0.1030 + 0.3555i) & (-0.2120 - 0.2120i) \\ (0.7987 + 0.2694i) & (-0.1064 + 0.2709i) & (-0.1671 - 0.0954i) & (0.0357 + 0.4080i) \\ (0.2852 + 0.2393i) & (-0.3399 - 0.2852i) & (0.1006 + 0.5704i) & (0.3290 - 0.4698i) \end{bmatrix} \tag{2.19}$$

$$W_{error} = \begin{bmatrix} (-0.2397 - 0.0108i) & (-0.1134 + 0.1782i) & (0.5099 + 0.4742i) & (0.1663 + 0.6207i) \\ (0.0837 + 0.3028i) & (0.7709 + 0.2727i) & (0.1029 + 0.3635i) & (-0.2210 - 0.2028i) \\ (0.7937 + 0.2745i) & (-0.1062 + 0.2805i) & (-0.1688 - 0.0916i) & (0.0498 + 0.4067i) \\ (0.2851 + 0.2392i) & (-0.3446 - 0.2794i) & (0.1120 + 0.5683i) & (0.3156 - 0.4792i) \end{bmatrix} \tag{2.20}$$

The percentage difference ($\Delta\%$) between W_{ideal} and W_{error} is calculated element-wise by taking the magnitude of the complex difference between the corresponding elements of the matrices. The formula used for each element (p, q), where p and q range from 1 to 4 for all

elements, is given by:

$$\Delta\%_{(p,q)} = \left| \frac{W_{ideal(p,q)} - W_{error(p,q)}}{W_{ideal(p,q)}} \right| \times 100 \tag{2.21}$$

The resultant difference percentage matrix ($M_{\Delta\%}$), is the following:

$$M_{\Delta\%} = \begin{bmatrix} \mathbf{6.3859} & \mathbf{6.1165} & 1.9365 & 0.0600 \\ \mathbf{4.5299} & 1.1038 & 2.1540 & \mathbf{4.2873} \\ 0.8516 & \mathbf{3.3016} & 2.1817 & \mathbf{3.4635} \\ 0.0600 & 1.6781 & 2.000 & 2.8564 \end{bmatrix} \tag{2.22}$$

This matrix revealed that for an inaccuracy of 2% in the beamsplitters of a 4×4 Reck topology, six elements of the weight matrix exhibit changes exceeding 3% for some of the matrix elements. In fact, two of these elements show a significant loss of up to 6%. The reported total power consumption of this MZI configuration is approximately 507 mW [3]. In this configuration, 12 directional couplers (DCs) are used. For a tunable directional coupler (TDC) with a 6 µm coupling length, the power required per TDC is 47 mW for a 50 µm heater length and 14 mW for a 10 µm heater length. The resulting temperature rise in the heaters remains within a safe range, as shown in Figure 2.4.

Therefore, the power consumption for 12 TDCs would be 564 mW for a 50 µm heater length and 168 mW for a 10 µm heater length. This brings the total power consumption of

the entire MZI configuration to approximately 1 W and 675 mW, respectively.

2.5 Summary

In this chapter, we reviewed the theoretical background of physical processes in silicon photonic (SiPh) switches, including the concepts of optical modes and mode multiplexing. We explored optical waveguides on silicon-on-insulator (SOI) structures, focusing on a rectangular silicon strip waveguide with a thickness of 220 nm. We discussed the relationship between the width of the strip waveguide and the guided optical modes. The design of titanium tungsten (TiW) heaters was examined by defining the thermal properties necessary for accurate simulation using commercial Ansys/Lumerical HEAT tool. We highlighted the linear relationship between the applied electrical power (P) to the metal heater and the wavelength shift ($\Delta\lambda$) in silicon waveguides. This relationship is crucial for designing the tunable directional couplers, as it directly relates the applied electric power to changes in the splitting percentage.

We then presented the theoretical background of directional couplers, focusing on the supermode theory approach for mode coupling between two waveguides. Graphical analysis showed that the TE1 mode has a stronger evanescent field in the gap between the coupling waveguides compared to the TE0 mode. This provides more flexibility in designing TE1 mode-selective tunable directional couplers (MS-TDCs). The stronger coupling of the TE1 mode also means it is more sensitive to the applied electric power than the TE0 mode. The

crossover length for complete optical power transfer was found to be approximately 19 µm for the TE1 mode and 200 µm for the TE0 mode, given a coupler gap of 200 nm.

We also discussed Mach-Zehnder interferometers (MZIs) in reconfigurable optical processors (ROPs). Each MZI has two beamsplitters, making ROP configurations highly dependent on the accuracy of these beamsplitters. We found that a 2% inaccuracy in directional coupler splitters applied to a 4×4 Reck topology results in up to a 6% loss of accuracy in the topology matrix elements, significantly impacting the overall accuracy of the ROP. These results motivate the need for tunable directional couplers that can compensate for fabrication errors to ensure accuracy in ROP configurations.

Chapter 3

Single-Mode Tunable Directional Coupler

Tunable directional couplers (TDCs) have diverse applications, including their use in tunable optical filters, where TDCs adjust the filter range by applying power [51]. They are also employed in switchable mode directional couplers, serving as switches to direct light to specific output ports [52]. Additionally, TDCs are crucial for adjusting the splitting ratio in reconfigurable optical processors (ROPs), which is the focus of this thesis. In the introduction chapter, we highlighted how fabrication process variations, particularly in phase shifters and directional coupler (DC) splitters, significantly impact ROPs, especially within the building blocks like Mach-Zehnder interferometers (MZIs). In the background chapter, we quantified the impact of a 2% error in the splitting percentage for MZI splitters in ROPs. We found

that 63% of the 4×4 weight matrix elements had changes greater than 2%, with two elements in the Reck topology experiencing up to 6% change in their value.

Various methods have been proposed to alleviate the sensitivity of conventional DCs to fabrication errors. These approaches include the use of tapered DCs [53] and adiabatic DCs [54]. However, implementing these techniques often creates additional design complexity. Tapered DCs require precise control over the tapering profile to ensure optimal performance, while the gradual transition required in adiabatic DCs can be challenging to fabricate with high precision. In addition, both designs need a larger footprint compared to conventional DCs. For example, the tapered DC in [53] and the adiabatic DC in [54] are 2600 µm and 100 µm, respectively, compared to our tunable DC of 6.5 µm.

There are also alternative methods to achieve tunable coupling ratios in DCs without relying on thermal heaters, offering improved power efficiency. One such approach is the use of micro-electromechanical systems (MEMS), where the DC consists of one movable arm and one fixed arm. By attaching an electrostatic comb-drive to the movable arm, the waveguide gap separation in the DC becomes tunable, resulting in an adjustable coupling ratio [55]. Another technique involves the use of phase-change materials (PCMs), such as $Ge_2Sb_2Te_5$ and Sb_2S_3, which can switch between amorphous and crystalline states. This phase transition alters the refractive index, enabling optical tuning without a continuous power supply [56]. However, these methods also introduce design challenges. MEMS-based DCs require precise mechanical structures, which can complicate fabrication and may raise

concerns about long-term reliability due to mechanical wear and sensitivity to environmental factors. Similarly, integrating PCM materials into DCs requires specialized deposition and patterning processes. Moreover, PCMs have a finite number of transition cycles between their amorphous and crystalline states before degradation occurs, limiting their lifespan [57].

Thermally tunable directional couplers (TDCs) offer a solution to rectify power imbalances encountered in directional couplers. This capability was first addressed through different proposed methods, including the integration of a 900 nm width asymmetrically placed heater above the DC coupling waveguides, enabling control over the tunability of the directional coupler [58]. However, its fabrication remains challenging as the tunability performance is sensitive to the precise alignment of the metal heater. Additionally, this design does not conform to the design rules of some standard silicon photonic foundries, with the metal heater width falling below the required minimum of 2 µm [30]. More recently, a thermally actuated dual-drive directional coupler has been proposed that incorporates two independent phase actuator heaters, one on each waveguide of the directional coupler. This setup allows for tuning the splitting ratio by either increasing or decreasing it, depending on the activated phase actuator [59]. These two designs are limited to single-mode operation and the literature does not report on possible solutions for mode-selective coupling.

3.1 Design and Simulation

The designed SM-TDC (Figure 3.1) exploits the SOI technology manufactured by Applied Nanotools (ANT) [30]. The silicon (Si) waveguides have a strip cross-section of 500 × 220 nm^2 and separated by 100 nm gap on a 2 µm silica (SiO_2) layer of buried oxide. The waveguides are then coated with a 2.5 µm layer of SiO_2 cladding to form the structure. The metal heater used in this design is of titanium tungsten (TiW) and is 200 nm thick. The heater is positioned 1.98 µm above the coupling waveguides of the TDC, and horizontally centered with respect to the coupling waveguides. Two heaters are designed with widths of 3 µm and 4 µm and lengths of 50 µm and 100 µm to investigate the impact of metal dimensions on the SM-TDC performance.

In our investigation, we initially employ simulation using Ansys/Lumerical MODE, specifically utilizing the finite difference eigenmode (FDE) solver, which calculates the coupling coefficient and the optical transmission for directional couplers based on the supermode approach previously discussed in section 2.3.1. The design consists of two straight waveguides separated by a 100 nm gap, as shown in Figure 2.5. This setup allow the calculation of mode field profiles and effective index estimations, providing relatively accurate results. Subsequently, we use Ansys/Lumerical 3D finite-difference time-domain (FDTD) simulation to accurately model and optimize the 3D structure of the SM-TDC depicted in Figure 3.1. Additionally, Ansys/Lumerical HEAT solvers is employed to investigate the effect of applied electric power on the heater temperature and subsequent to

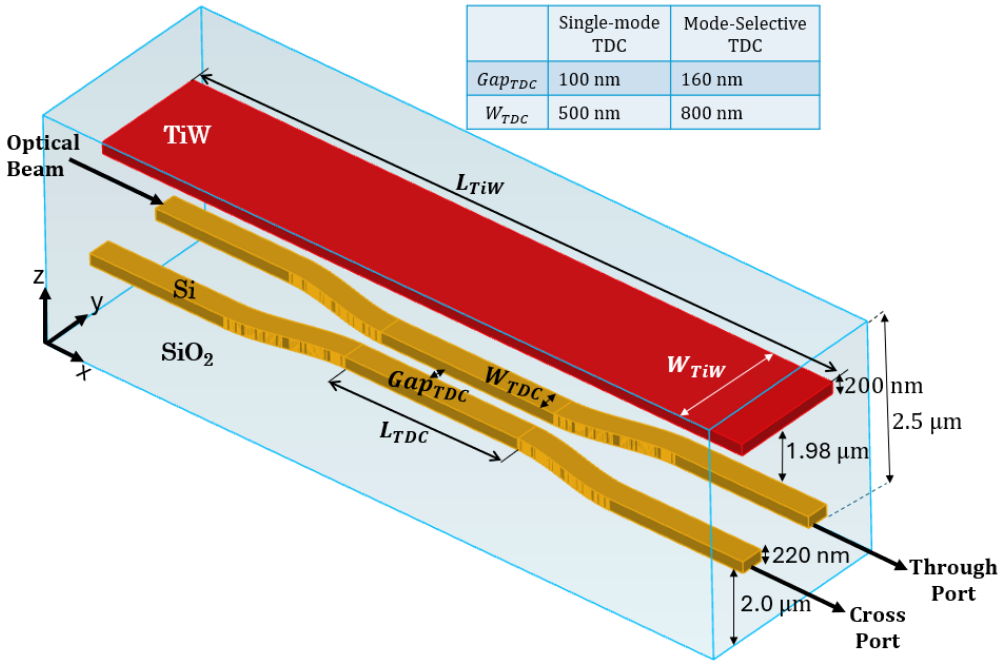

Figure 3.1: Schematic diagram of the designed TDC with its dimensions in the SOI technology platform, where L_{TiW} and W_{TiW} represent the length and width of the heater, respectively, and L_{TDC}, W_{TDC}, and Gap_{TDC} denote the coupling length, width, and gap of the coupler, respectively (dimensions not to scale).

the coupler waveguides though heat conduction. This analysis helps us understand the thermal response of the waveguides and the resulting effect on the coupling behavior.

The design of the SM-TDC requires both the coupling waveguide specifications and the heater specifications. For the coupling waveguide, a width of 500 nm is selected based on considerations discussed in the background section 2.1.2, ensuring the propagation of the single TE-like mode polarization, specifically the fundamental TE0 mode. A 100 nm gap is chosen to facilitate higher coupling, resulting in shorter crossover lengths. As shown in Figure 3.2, it is 13 µm at a wavelength of 1550 nm. This gap is larger than the minimum

spacing feature of 70 nm in the silicon layer of the ANT foundry.

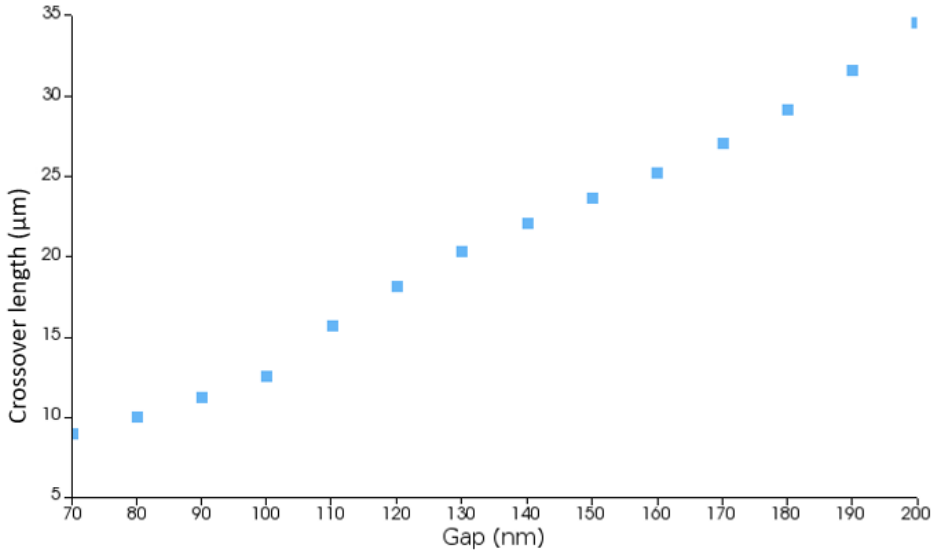

Figure 3.2: Simulation of crossover length of the TE0 mode versus coupler gap at 1550 nm for a 500 $\times$ 220 nm^2 waveguide.

In section 2.4, we discussed the importance of accurately adjusting MZI beamsplitters to achieve a 50:50 splitting ratio. Figure 3.3 illustrates the power transmission splitting percentage versus the coupling length for a SM-TDC with a 100 nm gap at a wavelength of 1550 nm. The propagation loss for the TE0 mode in straight waveguides fabricated by Applied Nanotools (ANT) is 1.5 dB/cm and 3.5 dB/cm for bends [30], which has a negligible effect on transmission due to the short lengths of our TDC. For instance, with a coupling length of 27 µm, the power transmission in the cross port is reduced from 1 to 0.998, accounting for propagation loss in both the straight coupling waveguide and bends.

The intended design aims to achieve tunability that surpasses the fabrication process

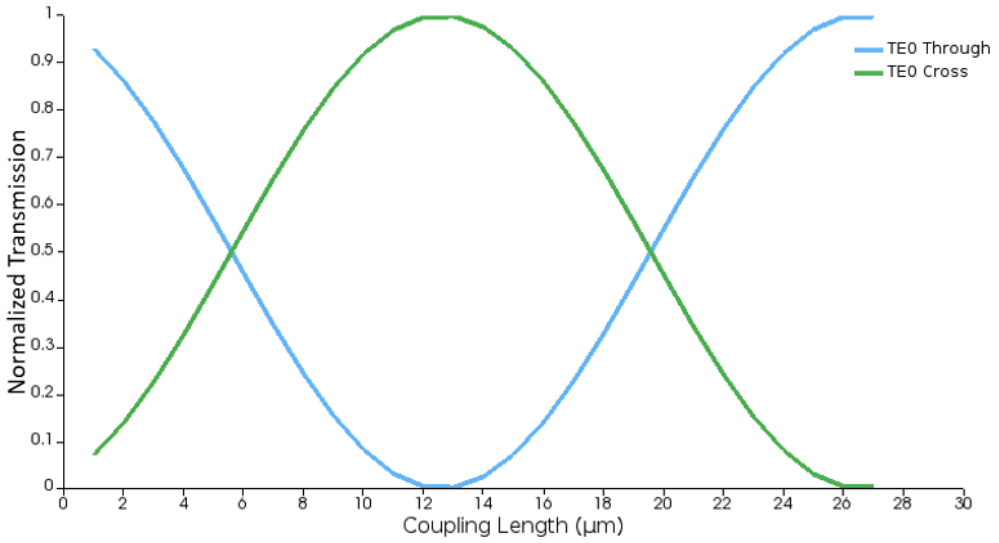

Figure 3.3: Simulation of the optical power transmission versus coupling length at a wavelength of 1550 nm for a SM-TDC with a 100 nm coupling gap.

variations occurring in the 50:50 splitting ratio of directional couplers. In our simulation, two specific lengths, 5.6 µm and 19.5 µm, meet this splitting ratio. Equation (2.1) shows that applying electrical power leads to a temperature change, resulting in a positive shift in wavelength towards longer wavelengths. This occurs because the positive thermo-optic coefficient implies an increase in the index of refraction with a temperature change. Thus, the SM-TDC is designed to achieve a 50:50 splitting ratio at a wavelength shorter than the desired wavelength of 1550 nm. By applying electrical power, the splitting percentage can be adjusted to reach the intended ratio at the target wavelength. This approach ensures precise control over the splitting ratio, compensating for fabrication process variations and enhancing the performance of the TDC.

Figure 3.4 shows the relationship between the coupling length required for a 50:50

splitting percentage and the wavelength. As observed, there is an inverse relationship where the coupling length for a 50:50 splitting percentage decreases with increasing wavelength. Consequently, to achieve a 50:50 splitting percentage at a wavelength of 1550 nm, the SM-TDC should be designed for a slightly shorter wavelength than 1550 nm, which corresponds to a coupling length slightly longer than the desired length at 1550 nm.

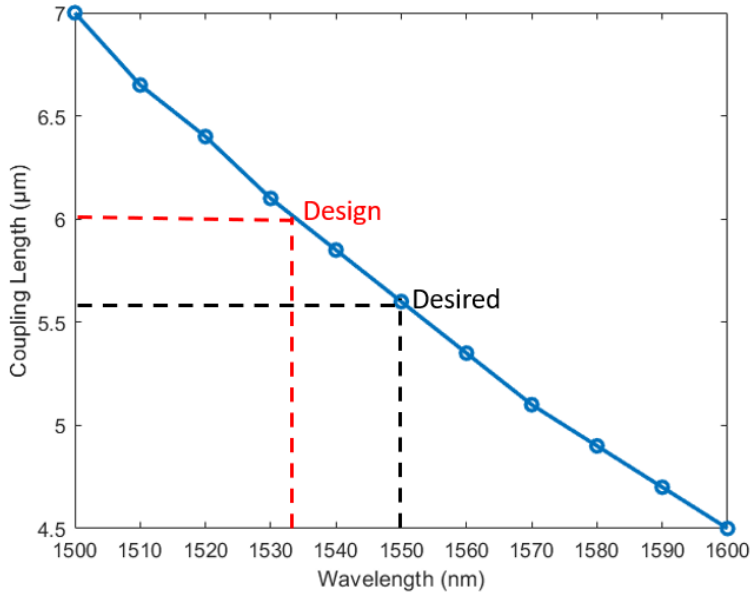

Figure 3.4: Simulation of the coupling length required for a 50:50 splitting versus wavelength for a SM-TDC. Highlighted are the desired 50:50 splitting point at a wavelength of 1550 nm, and the designed 50:50 splitting point at a wavelength of 1532 nm, corresponding to coupling lengths of 5.6 µm and 6 µm, respectively.

For example, a 6 µm coupling length is chosen by design, which is longer than the 5.6 µm length that represents the 50:50 splitting ratio at a wavelength of 1550 nm. At this longer coupling length, the 50:50 splitting ratio occurs at a wavelength around 1532 nm, which is at a shorter wavelength than the target wavelength of 1550 nm, as shown in Figure 3.5.

To achieve the desired splitting ratio at the target wavelength of 1550 nm, the appropriate amount of electric power is applied. This allows for precise tuning and shifting of the splitting ratio, ensuring optimal performance despite fabrication process variations.

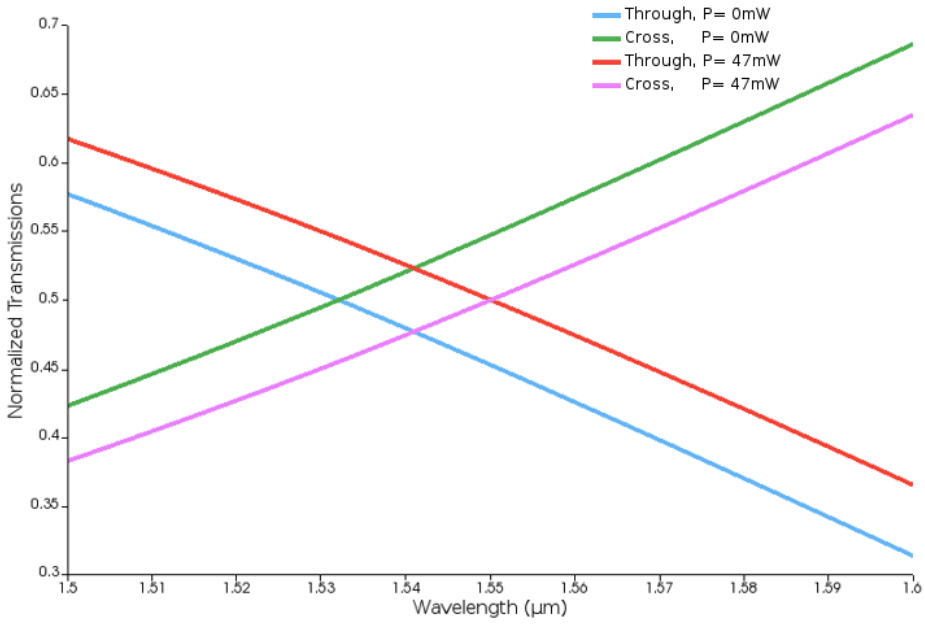

Figure 3.5: Simulation of optical power transmission versus wavelength for a SM-TDC with a 6 µm coupling length at different power levels (0 mW and 47 mW) for a heater length of 50 µm.

The tunability of the SM-TDC is linearly proportional to the temperature change at the coupling area, which can be controlled by applying power to the heater (Fig. 2.4). Applied Nanotools (ANT) specifies the maximum current density of a TiW heater, defining the maximum current allowed to flow through the heater before failure as 70 mA/µm^2. This information is used to determine the maximum applied current and thus the maximum

power applied to the heater. The maximum current flow is calculated as follows:

$$I_{\max} = J_{\max} \times (W_{\mathrm{TiW}} \times H_{\mathrm{TiW}})$$

where $I_{\max}$ is the maximum current flow through the heater in units of milliamperes (mA), $J_{\max}$ is the current density through the heater in units of milliamperes per micrometer squares (mA/µm^2), and W_{TiW} and H_{TiW} are the width and thickness of the heater in units of micrometers (µm), which together define the cross-sectional area of the heater. Our designs for both the single-mode TDC and mode-selective TDC use heaters with widths of 3 µm and 4 µm, and a heater thickness of 0.2 µm. Consequently, the $I_{\max}$ through the heater is 42 mA and 56 mA for heater widths of 3 µm and 4 µm, respectively.

The maximum power applied to the heater is calculated using the following equation:

$$P_{\max} = I_{\max}^2 \times R_{\mathrm{TiW}}$$

where R_{TiW} is the resistance of the heater, calculated as in Equation 2.5. The maximum allowable power before failure for heaters shown in Figure 2.4, is as follows:

- For a heater with dimensions $W_{\mathrm{TiW}} = 4$ µm and $L_{\mathrm{TiW}} = 10$ µm (black line), the maximum power is 24 mW.
- For a heater with dimensions $W_{\mathrm{TiW}} = 3$ µm and $L_{\mathrm{TiW}} = 50$ µm (red line), the maximum

power is 89 mW.

- For a heater with dimensions $W_{\mathrm{TiW}} = 4$ µm and $L_{\mathrm{TiW}} = 100$ µm (blue line), the maximum power is 238 mW.

Table 3.1 presents the amount of power needed to shift the 50:50 splitting point of the SM-TDC with a 6 µm coupling length from 1530 nm to 1550 nm for different heater lengths.

Table 3.1: Power required to shift the 50:50 splitting point to a wavelength of 1550 nm for 6 µm SM-TDC.

Heater length (µm)	Power (mW)
10	14
50	47
100	98

3.2 Experimental Setup

The experimental setup includes a C-band tunable laser as the continuous wave (CW) light source, capable of sweeping the output wavelength over a specified range. The output of the tunable laser is connected to a polarization controller, which adjusts the polarization state of the light to ensure optimal coupling into the photonic chip through the grating coupler, which is polarization-sensitive for the TE0 mode. At the output of the TDC, the light is split between two ports: the through port and the cross port (Fig. 3.1). Two optical power meters are used to simultaneously measure the optical power at these ports. These measurements are essential for determining the splitting ratio of the TDC and its tunability.

The TiW metal heater, integrated with the TDC, is controlled by a DC power supply, which operates as a current source limited to 35 mA and 45 mA instead of the theoretically rated current limits of 42 mA and 56 mA for heater widths of 3 µm and 4 µm, respectively, due to fabrication process variations that can cause the failure current to be lower than the rated value. The power supply regulates the electrical power supplied to the heater, which in turn adjusts the temperature of the coupling region. This temperature change modifies the effective refractive index and thereby the coupling ratio of the TDC.

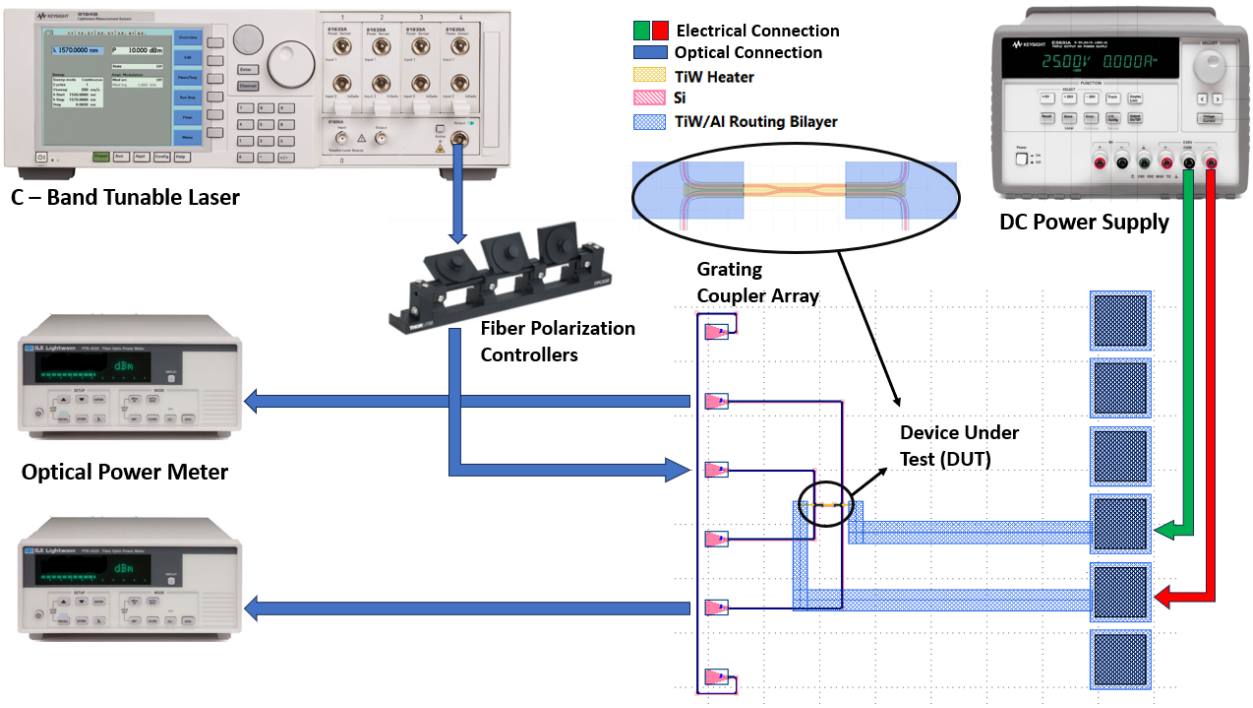

Figure 3.6: Experimental setup for a SM-TDC.

3.3 Experimental Results

Experimental measurements are conducted over various devices with a range of coupling lengths and heater dimensions. The initial experiment aims to validate the linear relationship between the wavelength shift ($\Delta\lambda$) of the 50:50 splitting ratio and the applied electrical power for two SM-TDCs with a coupling length of 6.5 µm, considering different heater lengths of 50 µm and 100 µm, and widths of 3 µm and 4 µm to study the effect of changing heater dimensions on wavelength shift and coupler tunability. Figure 3.7 compares the simulation and experimental data.

The experimental data for the SM-TDC with a coupling length of 6.5 µm demonstrates that a wavelength shift of 0.43 nm/mW is achieved using a heater with dimensions of 3 µm in width and 50 µm in length. A smaller wavelength shift of 0.19 nm/mW is achieved using a longer heater with dimensions of 4 µm in width and in 100 µm length. As such, a decrease in the heater dimensions leads to an increased wavelength shift, where the wavelength shift is linearly proportional to the temperature of the heater, and the power needed to increase the temperature for smaller heater dimensions is lower.

In simulation, a threefold improvement in wavelength shift efficiency is attained when the heater length is decreased to 10 µm.

Figure 3.8 illustrates the measured splitting ratio as a function of wavelength for both 0 mW and 20 mW applied power. The data is provided for two SM-TDC configurations: one with a coupling length of 5.5 µm and another with 6.5 µm coupling length, each featuring

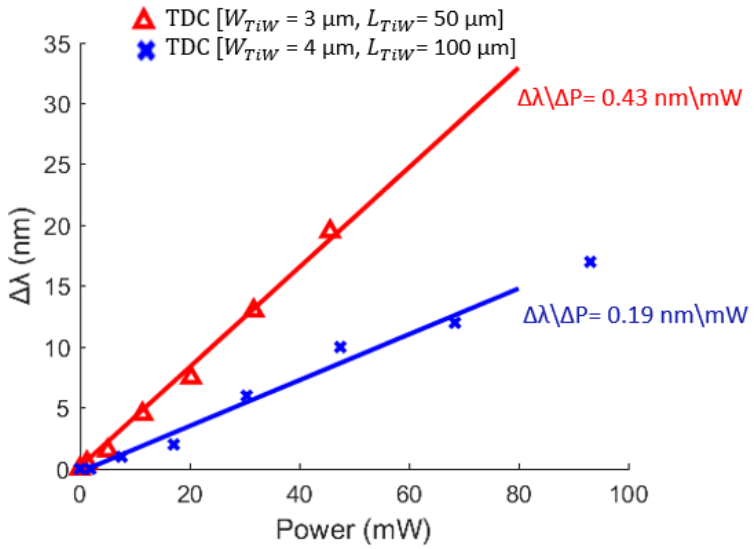

Figure 3.7: Wavelength shift ($\Delta\lambda$) of the 50:50 splitting ratio as a function of the applied electrical power for a coupling length of 6.5 µm, for two different heater designs.

different heater lengths (100 µm and 50 µm respectively). As depicted in the figure, the curve undergoes a shift towards longer wavelengths with applied power. If we hypothetically remove the wavelength shift between both curves, they should perfectly overlap. However, a vertical gap is observed between the scenarios with and without applied power. This discrepancy may be due to using a fiber array with a 10-degree incident light angle, while the grating couplers are designed for an 8-degree angle. The lack of a matching fiber array leads to refraction and reflection effects, which might be causing this gap.

To shift the 50:50 splitting ratio from 1511 nm when 0 mW power is applied to 1550 nm with a coupling length of 6.5 µm, it requires an electrical power exceeding 45 mW. Using experimental results from Figure 3.7, the measured slope ($\frac{\Delta\lambda}{\Delta P}$) can predict the amount of power required to reach the 50:50 splitting point at 1550 nm, as shown in the following

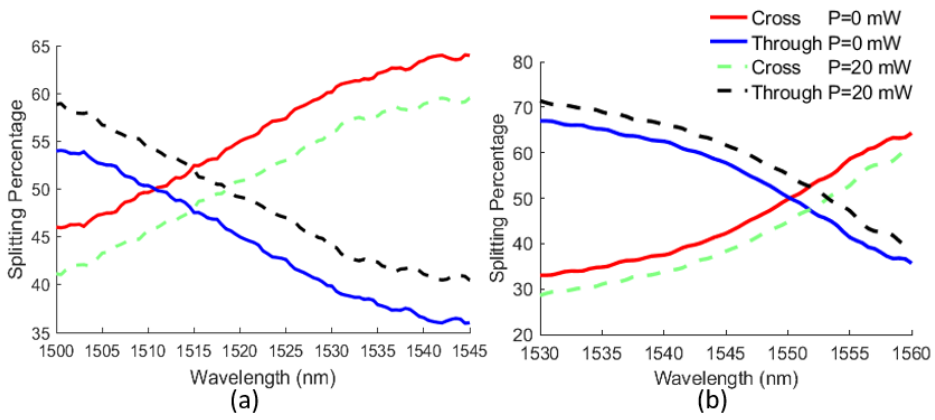

Figure 3.8: Measured change in the splitting ratio as a function of wavelength under two conditions: without the application of electrical power and with 20 mW of power applied, (a) for the SM-TDC with a coupling length of 6.5 µm, and heater dimensions of 3 µm in width and 50 µm in length; (b) for the SM-TDC with a coupling length of 5.5 µm, and heater dimensions of 3 µm in width and 100 µm in length.

equation:

$$P_{\text{required}} - P_{0W} = \frac{\lambda_{\text{required}} - \lambda_{0W}}{\frac{\Delta\lambda}{\Delta P}} \tag{3.1}$$

where P_{required} is the required power to shift the 50:50 splitting ratio from the initial wavelength λ_{0W} when no power P_{0W} is applied to the required wavelength $\lambda_{\text{required}}$. By applying the given values, the required power can be calculated as:

$$P_{\text{required}} = \frac{1550 - 1511}{0.43} = 91 \text{ mW}$$

The required power of 91 mW to shift the 50:50 splitting ratio for a SM-TDC with a coupling length of 6.5 µm to 1550 nm, using heater dimensions of 3 µm in width and 50 µm

in length, represents the maximum allowed power for those heater dimensions. Alternatively, selecting a shorter coupling length of 6 µm results in a 50:50 splitting ratio at 1532 nm in simulations. To achieve the same 50:50 splitting ratio at 1550 nm, an electrical power of 47 mW is required, as detailed in Table 3.1.

To design a SM-TDC that achieves a 50:50 splitting ratio at a specific desired wavelength, such as 1520 nm, the design should target a 50:50 splitting ratio at a shorter wavelength. At the same time, it should have at least a 3% to 4% deviation from 50:50 at the desired wavelength (1520 nm) before applying power, exceeding the possible fabrication-induced splitting deviations in SOI directional couplers, which may fall within the range of ±2% to ±3% [48]. For example, to achieve a 50:50 splitting ratio at 1520 nm, the design should target a 50:50 splitting ratio at 1511 nm, which is shorter than 1520 nm and has a 52:48 splitting ratio at 1520 nm, reflecting a deviation of 4% from the 50:50 splitting percentage at 1520 nm before applying power. By applying an electrical power of 20 mW, the 50:50 splitting ratio shifts from 1511 nm to 1520 nm (Fig. 3.8a).

The experimental data, shown in Figure 3.9, depict the splitting ratio response of the two SM-TDCs to applied power at a specific wavelength. For the SM-TDC with a coupling length of 6.5 µm and a 50 µm heater length, the splitting ratio for the through port changes from 50% to 60% for an electrical power varying from 0 to 45 mW. Simultaneously, the cross port splitting ratio changes from 50% to 40%, indicating a tunability of up to 10% in the splitting ratio at a specific wavelength. However, for a coupling length of 5.5 µm, the

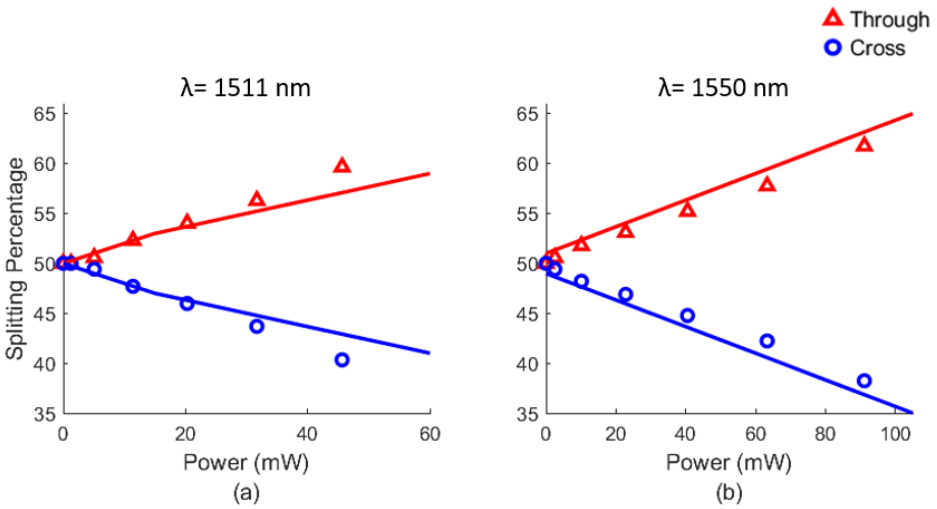

Figure 3.9: Measured change in the splitting ratio of the SM-TDC as a function of applied electrical power at a specific wavelength. Configuration (a) corresponds to a coupling length of 6.5 µm, with a heater width and length of 3 µm and 50 µm, respectively, at a wavelength of 1511 nm. Configuration (b) represents a coupling length of 5.5 µm, featuring a heater width and length of 3 µm and 100 µm, respectively, at a wavelength of 1550 nm.

tunability is reduced to 5% for the same power range for a heater length of 100 µm. If the heater length is decreased to 10 µm, the tunability can extend to 30% for the same amount of power.

3.4 Summary

This chapter aims to introduce a single-mode tunable directional coupler (SM-TDC) designed to compensate for fabrication process variations. The design of the SM-TDC begins with specifying the silicon coupling waveguides' length, width, and the gap separating them. The

width of the coupling waveguide is 500 nm, ensuring the propagation of the fundamental TE0 mode. The gap is 100 nm to facilitate high coupling, resulting in a short crossover length of 13 µm at a wavelength of 1550 nm. The coupling length used in simulations and experiments is longer than the length required for a 50:50 splitting ratio at 1550 nm, resulting in at least a 4% deviation from the ideal 50:50 splitting ratio. This is based on the discussion in this chapter, which demonstrates that to design a TDC to achieve a 50:50 splitting ratio at a wavelength of 1550 nm, the TDC should be designed for a slightly shorter wavelength than 1550 nm. This corresponds to a coupling length slightly longer than the desired length at 1550 nm. Additionally, it should exhibit a deviation of at least 4% from the ideal 50:50 splitting ratio at 1550 nm before applying power.

This chapter also discusses the design of the TiW heater and how to determine the maximum applied current and power before failure, based on the maximum current density ratings provided by the manufacturer. We found that the maximum allowed current through the heater depends on its width and is 42 mA and 56 mA for heater widths of 3 µm and 4 µm, respectively. The maximum allowed power is calculated as the maximum allowed current squared, multiplied by the heater resistance, which depends on the heater's width and length.

Our experiments validate the linear relationship between the wavelength shift ($\Delta\lambda$) of the 50:50 splitting ratio and the applied electrical power for two SM-TDCs with a coupling length of 6.5 µm. A wavelength shift of 0.43 nm/mW is achieved using a heater with dimensions

of 3×50 µm^2, and a wavelength shift of 0.19 nm/mW is achieved using a heater with dimensions of 4×100 µm^2. Thus, a decrease in the heater dimensions leads to an increased wavelength shift, as the power needed to increase the heater temperature is lower for smaller heater dimensions.

We found a tunability of up to 10% in the splitting ratio at a specific wavelength for SM-TDCs with a coupling length of 6.5 µm, using a heater with dimensions of 3×50 µm^2 for an electrical power varying from 0 to 45 mW. In simulation, for the same coupling length of 6.5 µm, the tunability can extend to 30% for the same amount of power if the heater length is decreased to 10 µm.

Chapter 4

Mode-Selective Tunable Directional Coupler

The mode-selective tunable directional coupler (MS-TDC) is designed to propagate both the fundamental transverse electric optical mode (TE0) and the first-order transverse electric optical mode (TE1). It has the capability to selectively couple the TE1 mode with different coupling ratios by adjusting the applied electrical power to the heater above the coupling waveguides, without affecting the TE0 mode, which entirely continues to pass through the through port.

Figure 4.1 represents the schematic diagram of the MS-TDC, and Figure 4.2 illustrates the mode-selective tunability of the MS-TDC with a 30 µm coupling length when power is applied. At 0 mW, both TE0 and TE1 modes propagate through the through port. As the

applied power is gradually increased, the TE1 mode starts to couple into the cross port. When the applied power reaches 110 mW, which is around the maximum allowed power for the heater before failure, the TE1 mode achieves a 50:50 splitting ratio between the through and cross ports, while the TE0 mode continues to propagate through the through port. As the power increases further, the coupling ratio of the TE1 mode to the cross port increases until it reaches 260 mW, at which point the TE1 mode is completely coupled to the cross port, while TE0 mode remains unchanged.

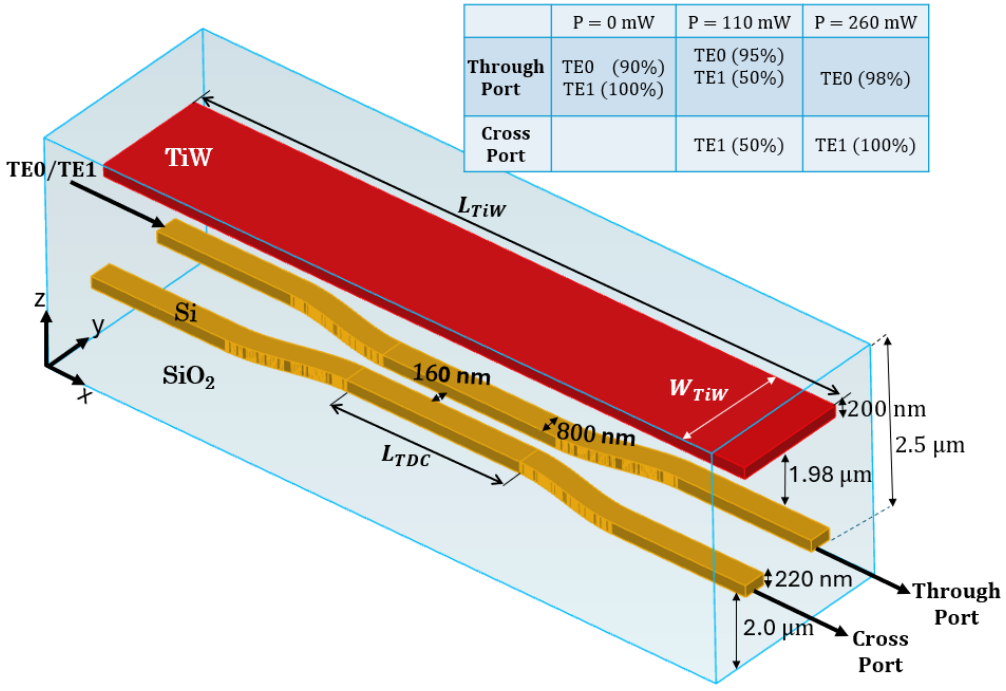

Figure 4.1: Schematic diagram of the designed MS-TDC with its dimensions in the SOI technology platform, where L_{TiW} and W_{TiW} represent the length and width of the heater, respectively, and L_{TDC} denotes the coupling length of the coupler. The table data represent the modes propagating in that port with their power transmission percentage when L_{TDC}= 30 µm (dimensions not to scale).

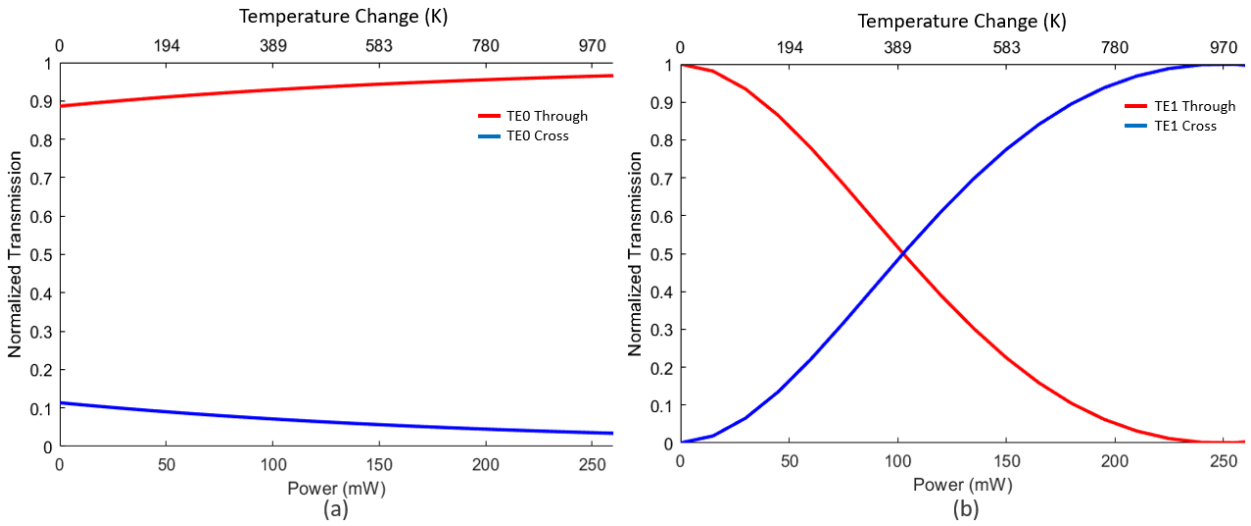

Figure 4.2: Simulation of optical transmission versus electrical power applied to the MS-TDC, indicating the change in temperature of the coupling waveguide relative to 300 K with a coupling length of 30 µm and a gap of 160 nm at 1550 nm for two modes: (a) TE0 mode, (b) TE1 mode.

4.1 Design and Simulation

The schematic design of the mode-selective TDC is presented in Figure 4.1, which shares a similar design to the single-mode TDC with some key differences. The waveguides have a width of 800 nm to support both TE0 and TE1 modes (Fig. 2.2). The gap between the waveguides is increased to 160 nm to achieve a separation that makes it harder for the TE0 mode to couple and easier for the TE1 mode to couple. The crossover length, where optical power is entirely transferred to the cross waveguide, is approximately 13.5 µm for the TE1 mode and 145 µm for the TE0 mode, as illustrated in Figure 2.8. This difference arises because the TE0 mode is more confined to the waveguide than the TE1 mode.

Consequently, the TE1 mode has a stronger overlap of the evanescent electric field compared to the TE0 mode, making the TE1 mode more prone to couple and exhibiting a tunable coupling behavior with changes in power, while the TE0 mode remains largely unaffected.

Figure 4.3 illustrates the relationship between the optical power transmission and the coupling length for the MS-TDC. Figure 4.3(a), almost all optical power of the TE0 mode is bypassed in the through port across the entire coupling length range. Figure 4.3(b), the coupling percentage for the TE1 mode varies between the through and cross ports in a sinusoidal pattern with respect to the coupling length, as discussed in Equations (2.9) and (2.10).

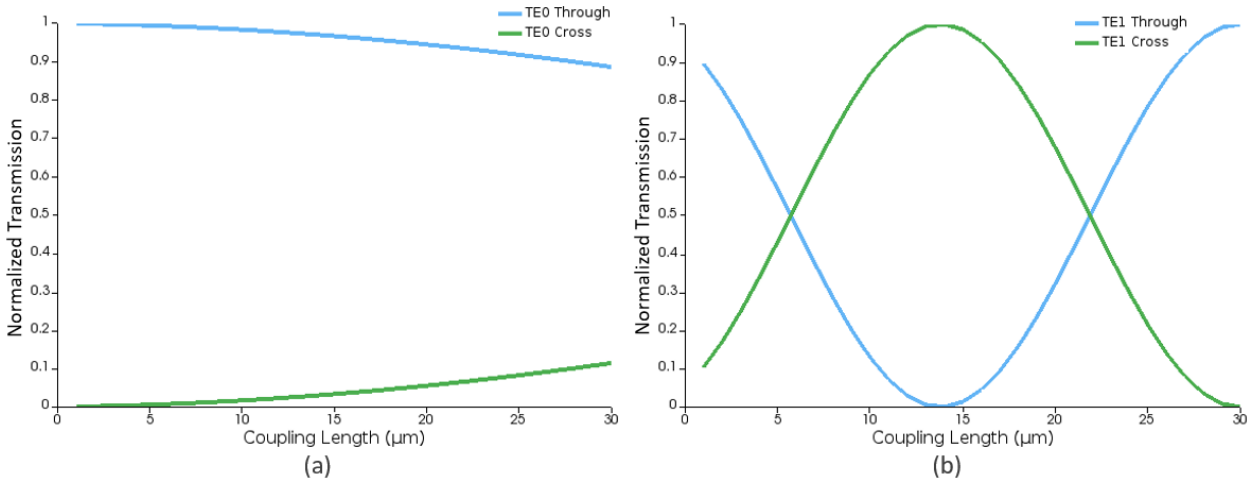

Figure 4.3: Simulation of optical power transmission versus coupling length at a wavelength at 1550 nm with a 160 nm coupling gap for MS-TDC: (a) TE0 mode, (b) TE1 mode.

Three specific design points are of particular interest:

1. 50:50 splitting of TE1 mode at 5.6 µm: At this coupling length, the optical power of the TE1 mode is evenly split 50:50 between the through and cross ports, while the TE0 mode power continues to propagate entirely through the through port.

2. Complete transfer of TE1 mode at 13.5 µm: At this coupling length, the optical power of the TE1 mode is entirely transferred to the cross port, reflecting the crossover length for the TE1 mode. This point is important in the design because it depicts the (de)multiplexer device of on-chip MDM systems capable of splitting or combining TE0 and TE1 modes.

3. 50:50 splitting of TE1 mode at 22 µm: Similar to the 5.6 µm point, at 22 µm, the optical power of the TE1 mode is again evenly split 50:50 between the through and cross ports, with all TE0 mode power in the through port.

These design points highlight the flexibility and potential of the MS-TDC in various applications, including on-chip MDM systems and reconfigurable optical processors (ROPs).

When an optical signal is injected into one arm of the MS-TDC along the x-axis (Fig. 4.1), the electric field is polarized along the y-axis direction for TE mode (Fig. 4.4). In Figure 4.4 three distinct coupling lengths are chosen: 5.6 µm, 13.5 µm, and 22 µm. The first row represents the electric field distribution for the TE0 mode, which remains uncoupled and propagates through the through port for all represented coupling lengths. The second row

represents the electric field distribution for the TE1 mode. The electric field is split evenly between the through and cross ports for both 5.6 µm and 22 µm coupling lengths, and the electric field is fully coupled to the cross port for the 13.5 µm coupling length.

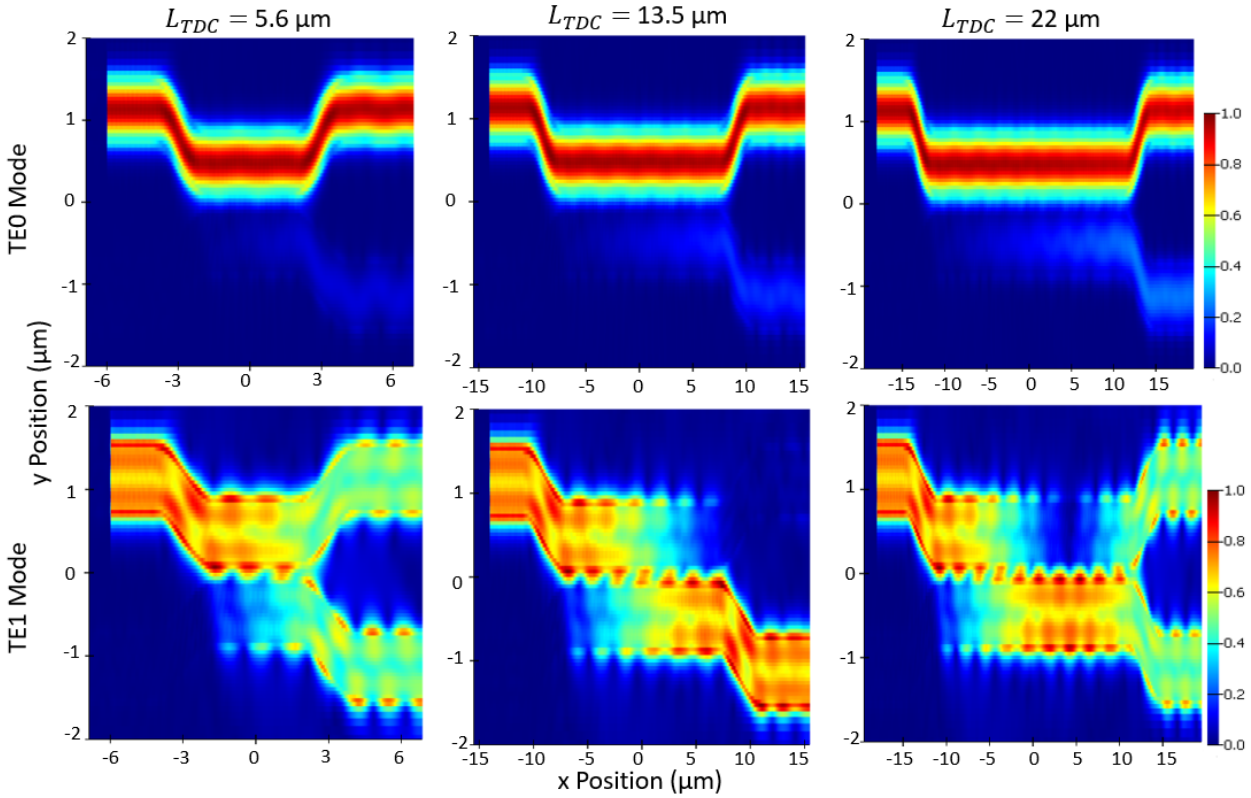

Figure 4.4: Simulation of the electric field distribution in MS-TDC couplers for three different coupling lengths: 5.6 µm (left column), 13.5 µm (middle column), and 22 µm (right column). The top row shows the distribution for the TE0 mode, while the bottom row shows the distribution for the TE1 mode.

Figure 4.4 also illustrates the concentration and strong confinement of the electric field for the TE0 mode to the core of the waveguide, represented by the darkest red. In contrast, the electric field for the TE1 mode is concentrated at the edges of the waveguide and shows a

strong evanescent electric field in the gap between the waveguides. This explains the stronger coupling for the TE1 mode compared to the TE0 mode.

As discussed in Section 3.1, to address fabrication process variations in directional couplers, the design should target a splitting percentage at a shorter wavelength than the desired wavelength, which implies a longer coupling length than the estimated length. For instance, we selected coupling lengths of 6 µm, 15 µm, and 23 µm through simulation, which are greater than the coupling lengths of 5.5 µm, 13.5 µm, and 22 µm, respectively. The 50:50 splitting ratio for the 6 µm and 23 µm coupling lengths occurs at a wavelength of 1541 nm, and at the same time, their 50:50 splitting ratio deviation at 1550 nm is greater than 4% before applying power. Full optical power transfer to the cross port for the 15 µm coupling length occurs at a wavelength of 1540 nm.

Table 4.1: Power requirements for the MS-TDC to shift the 50:50 splitting point for coupling lengths of 6 µm and 23 µm from 1541 nm to 1550 nm, and to shift the full coupling point for a 15 µm coupling length of the TE1 mode from 1540 nm to 1550 nm, for different heater lengths.

Coupling Length (µm)	Heater Length (µm)	Power (mW)
6	10	6
	50	14
15	10	15
	50	30
23	10	7
	50	17

Table 4.1 presents the power requirements to shift the 50:50 splitting point of the TE1 mode with coupling lengths of 6 µm and 23 µm from 1541 nm to 1550 nm. It also shows the

power needed to shift the full optical power transfer point of TE1 for the 15 µm coupling length from 1540 nm to 1550 nm at various heater lengths.

4.2 Experimental Setup

it is crucial to note that the C-band tunable laser used as the continuous wave (CW) light source generates only TE0 mode. While the MS-TDC uses both TE0 and TE1 modes. Figure 4.5 illustrates the schematic of the TE mode (de)multiplexer that has been presented by [22] and then demonstrated by our research team [18]. This structure comprises four input ports with varying waveguide widths, all excited with the TE0 mode. The top and bottom waveguides convert the TE0 mode into the TE1 mode, while the TE0 mode in the middle arms maintains its mode order.

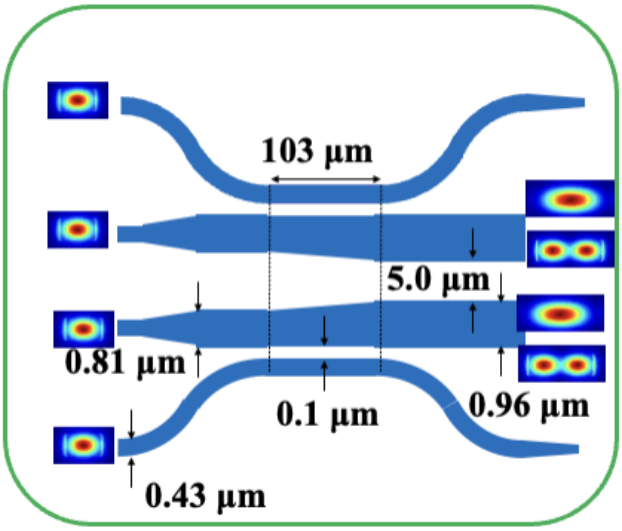

Figure 4.5: Schematic of the TE mode (de)multiplexer (dimensions not to scale).

The experiment requires two instances of this structure, as depicted in Figure 4.6. The first from the left operates as a multiplexer and a mode converter, connected to the output of the C-band tunable laser and before the input of the MS-TDC. It converts TE0 to TE1 for the top and bottom waveguides, then couples them to the main middle waveguides and directing the combined wave to the MS-TDC. At the output of the MS-TDC before the input of the optical power meters, the second instance operates as a demultiplexer and a mode converter. It separates the two modes, then converts TE1 for the top and bottom waveguides to TE0 for measurement.

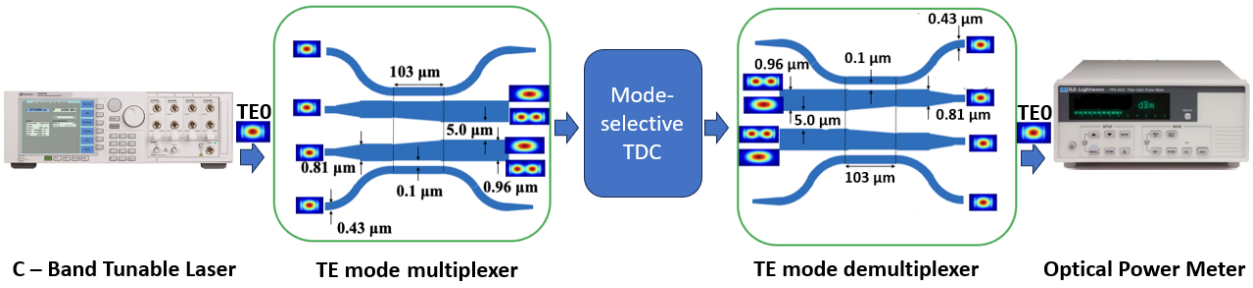

Figure 4.6: Schematic displays the TE0 and TE1 modes conversion and (de)multiplexing through the measuring circuit components.

The experimental setup, illustrated in Figure 4.7, closely resembles the setup used for the single-mode TDC, presented in section 3.2, with a few distinctions. Notably the two instances of mode (de)multiplexer structures added before and after the mode-selective TDC instance. There are also two grating coupler interfaces for each input, through, and cross ports, with one interface for TE0 mode and another for TE1 mode.

The setup simultaneously employs two optical power meters, which are connected to

the TE0 ports of the through and cross ports when measuring TE0 mode optical power. Similarly, then they are connected to the TE1 ports of the through and cross ports when measuring TE1 mode optical power. This configuration allows for the measurements of both TE0 and TE1 mode optical powers.

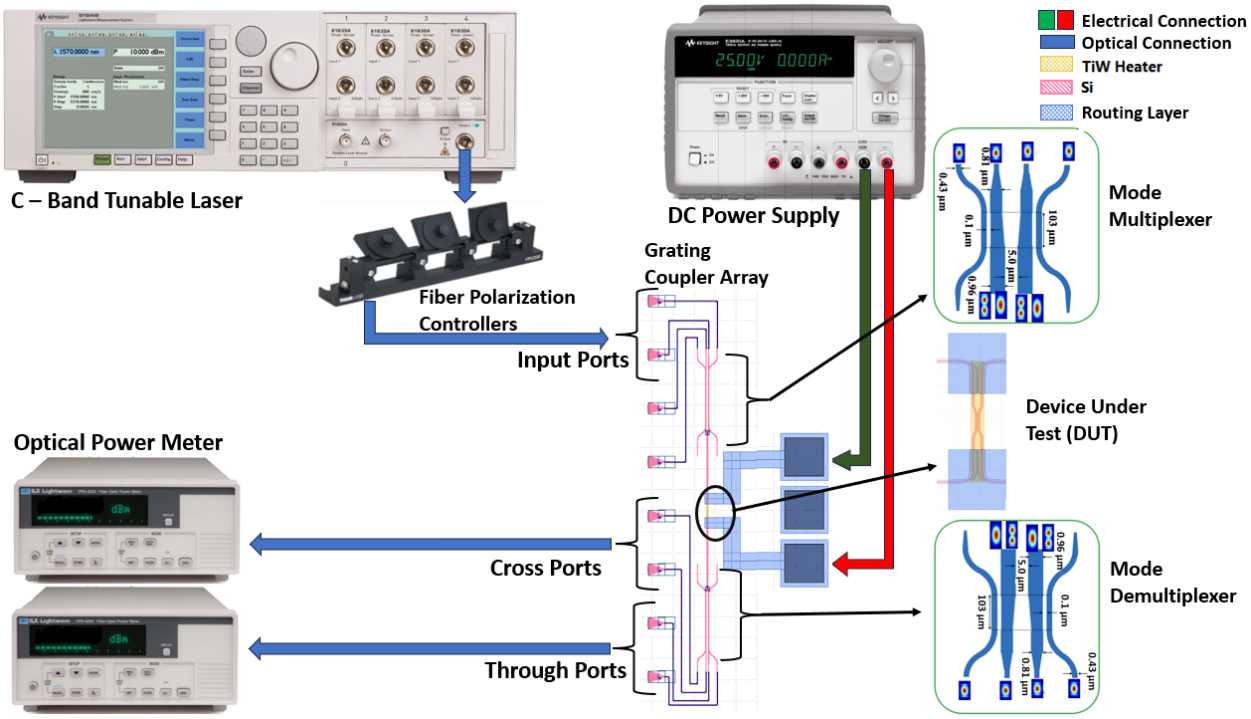

Figure 4.7: The full schematic of the MS-TDC measuring circuit.

4.3 Experimental Results

The experiments aim to validate the tunability of the 50:50 splitting point of the mode-selective TDC (MS-TDC) when applying electrical power to two designs featuring coupling lengths of 6.5 µm and 23 µm. Unfortunately, we did not include designs for coupling lengths

that are slightly longer than the TE1 mode crossover length of 13.5 µm of the MS-TDC in our layout, which can be used for experimenting with the tunability of the full optical power transfer point.

All three designs, two for the 50:50 splitting ratio and one for the full optical power transfer, share identical characteristics and conditions, including waveguide width, gap, and losses, with the only difference being the coupling length. Considering that forthcoming experimental results have validated the simulation outcomes for both shorter and longer lengths than the full optical power transfer length, it can be concluded that the simulation results presented in the previous section are reliable and trustworthy.

The experimental data presented in Figure 4.8 demonstrates a linear relationship between the wavelength shift ($\Delta\lambda$) and the 50:50 splitting ratio as a function of applied electrical power for TE1 mode. This alignment along with the findings in equation 2.1 facilitates control over the tunability of MS-TDC.

In Figure 4.9 the splitting ratio measurements are presented as a function of wavelength for two MS-TDCs of different coupling lengths under two conditions: no power and power required for a 50:50 splitting ratio at 1550 nm. As seen in the figure, the MS-TDC with a coupling length of 6.5 µm needs 46 mW to shift the 50:50 splitting ratio from 1533 nm to 1550 nm. The MS-TDC with a coupling length of 23 µm needs 15.5 mW to shift the 50:50 splitting ratio from 1542.5 nm to 1550 nm.

The results confirm that the TE1 mode exhibits tunable coupling behavior with its

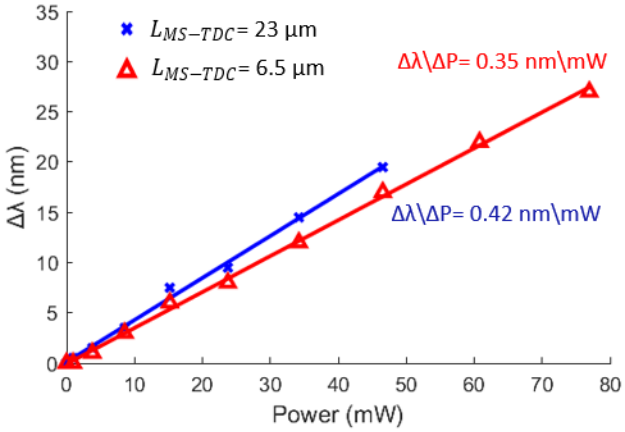

Figure 4.8: Wavelength shift ($\Delta\lambda$) of the 50:50 splitting ratio for TE1 mode as a function of applied electrical power for coupling lengths of 6.5 µm and 23 µm. The heater length is 50 µm and the width is 4 µm.

splitting ratio changing in response to applied power, while the TE0 mode remains uncoupled and insensitive to applied power variations. We observed the same vertical gap between the scenarios with and without applied power for both MS-TDCs, similar to the single-mode TDCs shown in Figure 3.8. We believe the reason for this discrepancy is the angle mismatch between the fiber array used, which has a 10-degree incident light angle, and the grating couplers, which are designed for an 8-degree angle.

Figure 4.10 reports the experimental change in the splitting ratio for the two MS-TDCs at specific wavelengths, each with a 50 µm heater length. Over an electrical power range of 0 to 45 mW, a tunability of up to 10% in the splitting ratio is attained for a coupling length of 6.5 µm, while a tunability of 25% is observed for a coupling length of 23 µm. This enhanced tunability is directly linked to the length of the coupling waveguides (L_{TDC}). As indicated

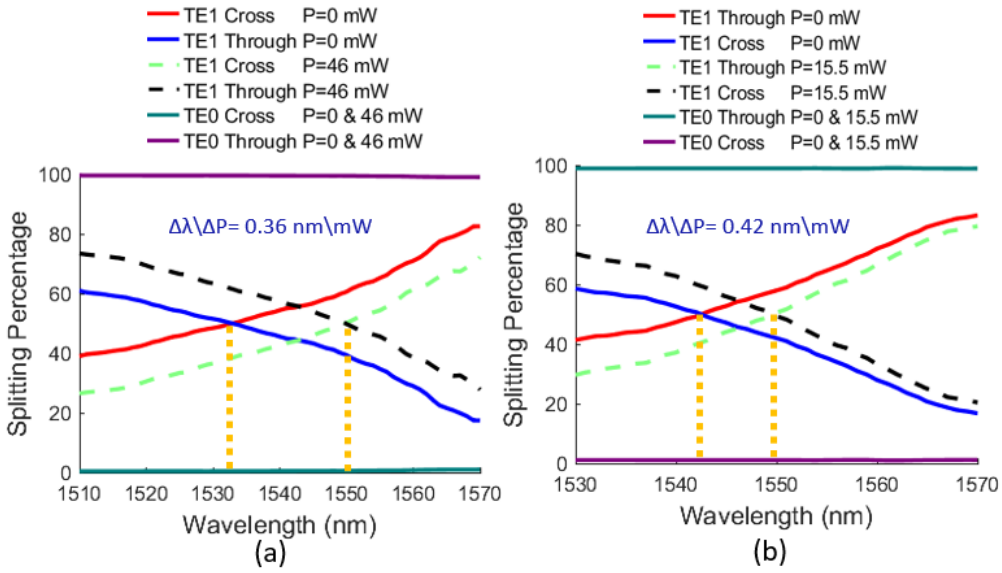

Figure 4.9: Measured change in the splitting ratio as a function of wavelength for two MS-TDC designs under two conditions: without the application of electrical power, and with the application of power needed for 50:50 splitting to reach 1550 nm, using heater dimensions of 4 µm in width and 50 µm in length. The measurements are conducted for both TE0 and TE1 modes, and include data for (a) a coupling length of 6.5 µm, as well as for (b) a coupling length of 23 µm.

in Eq. 2.9 and Eq. 2.10, the splitting ratio of coupling power depends on both L_{TDC} and the coupling coefficient (C), which can be directly controlled by applying power. This is because the coupling coefficient depends on the change in effective refractive index, which linearly changes with temperature, as indicated in Equation 2.1. Applying the same power to both couplers excludes the effect of the coupling coefficient (C), making the tunability of the coupler directly proportional to the length L_{TDC}. Theoretically, increasing the coupling length to 40 µm while maintaining the same heater dimensions and power rating could enhance tunability up to 35%.

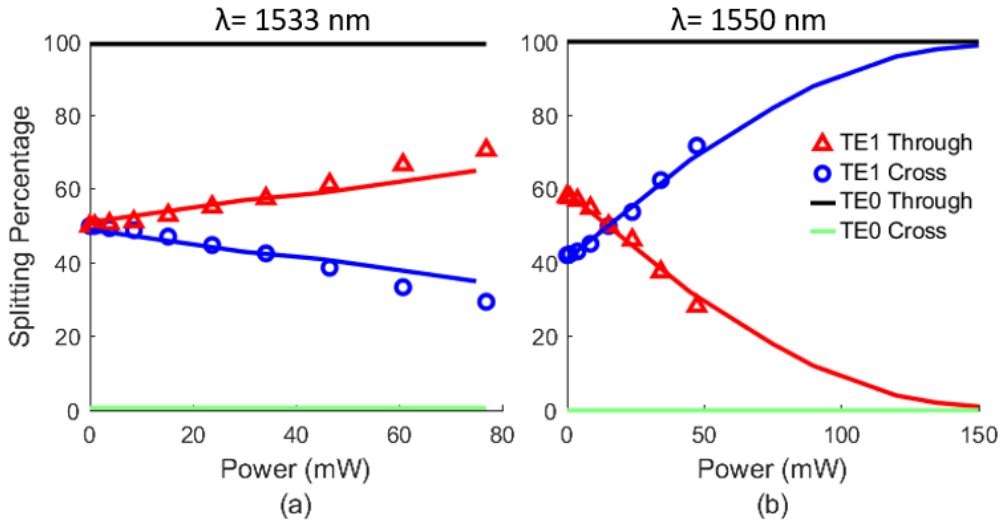

Figure 4.10: Measured change in the splitting ratio of the MS-TDC with respect to applied electrical power at a specific wavelength, using a heater with dimensions of 4 µm width and 50 µm length. Configuration (a) corresponds to a coupling length of 6.5 µm at 1533 nm. Configuration (b) represents a coupling length of 23 µm at 1550 nm.

From Figure 4.10, the relationship between the change in the splitting ratio and the applied power at a specific wavelength is not linear; instead, it follows a sinusoidal form because both the coupling coefficient and the coupling length are within a sinusoidal function, causing their response to behave as a sinusoidal wave (Eq. 2.9).

4.4 Future Work

In this section, we extend the designs of the tunable directional coupler (TDC) to cover a wide range of cases, enhancing the control over TE modes. Table 4.2 shows four possible designs of TDCs that manipulate and control the splitting ratio of the fundamental transverse electric

optical mode (TE0) and the first-order transverse electric optical mode (TE1). The first two designs have been discussed, simulated, and experimented, while the next two designs will be discussed and simulated in this section. These TDC designs significantly expand the potential applications of reconfigurable optical processors (ROPs) by enabling processing of not just the single TE0 mode, but also facilitating the development of two-mode ROPs. Recently, a mode-selective phase shifter in a Mach-Zehnder interferometer (MZI) has been experimentally demonstrated to manipulate both TE0 and TE1 modes [60]. These TDCs can also be applied in interferometric optical sensors to detect changes in TE0 and TE1 modes, similar to existing sensors that utilize TE0 and TM0 modes [61].

Table 4.2: Multi-mode directional coupler designs, where the splitting ratio is represented as a ratio of the through port over the cross port.

Design	TE0	TE1
Design 1	100:0	50:50
Design 2	100:0	0:100
Design 3	50:50	100:0
Design 4	50:50	50:50

4.4.1 TE0 Mode Selective 3 dB Splitter

This design is based on the schematics proposed in Figure 4.1, but with some modifications. The waveguides in this design have a width of 810 nm, chosen to support both TE0 and TE1 modes. The gap between the waveguides is 110 nm. These dimentions have crossover length of 91 µm for the TE0 mode and 9 µm for the TE1 mode. This means at a coupler length

equal to half the TE0 mode crossover length, there is a 50:50 splitting of optical power for the TE0 mode. Additionally, for coupler lengths that are multiples of the TE1 mode crossover length, there is a complete optical power transfer.

Figure 4.11 (a,b) illustrates the relationship between transmission splitting ratio and coupling length for this configuration at a wavelength of 1550 nm. At a coupling length of 44.5 µm, the TE0 mode exhibits a 50:50 splitting of optical power, while at the same length, the TE1 mode allows all the optical power to propagate through the through port. With these observations, all parameters for the design are determined: the waveguides' width, the gap, and the length of the coupler.

To demonstrate the tunability of the design to compensate for fabrication variations, a longer coupling length of 47 µm is chosen. This implies that the 50:50 splitting power point of the TE0 mode occurs at a wavelength of 1533 nm when no power is applied, which is shorter than the desired wavelength of 1550 nm for our target design. At the same time, it has a 45:55 splitting ratio for the TE0 mode at 1550 nm, reflecting a deviation greater than 4% from the 50:50 splitting ratio at 1550 nm before applying power. Figure 4.11 (c,d) shows that applying 25 mW of power is required to tune the 50:50 splitting power point of the TE0 mode to a wavelength of 1550 nm, while allowing 99% of the TE1 mode optical power to pass through the through port.

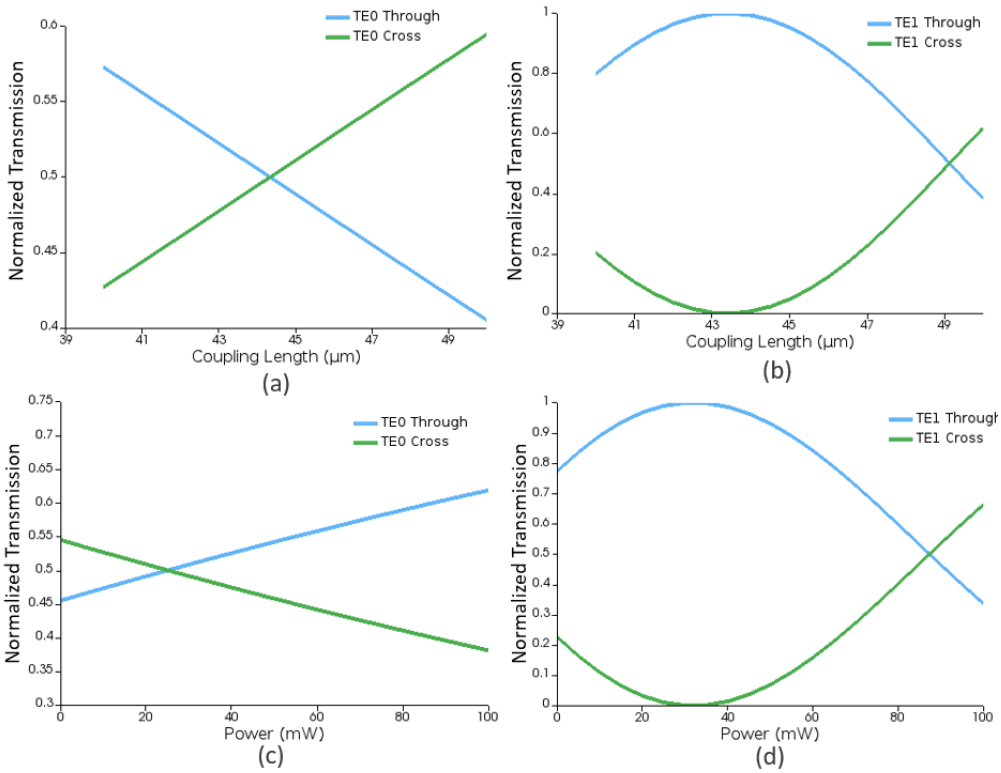

Figure 4.11: Simulations of transmission for a TDC with a 110 nm coupling gap and 810 × 220 nm² waveguides at 1550 nm: (a,b) versus coupling length for TE0 and TE1 modes, respectively, and (c,d) versus power for a coupling length of 47 µm for TE0 and TE1 modes, respectively.

4.4.2 Both Modes 3 dB Splitter

For both modes to split 50:50, the waveguides are widened to 860 nm, effectively enhancing the confinement of both TE0 and TE1 modes to the core of the waveguides. To achieve the desired coupling length at manageable values, the coupling gap is consequently reduced to 100 nm. This design achieves a 50:50 splitting ratio for both TE0 and TE1 modes at a coupling length of 42 µm at a wavelength of 1550 nm.

To validate the tunability over fabrication process variations, a longer coupling length of 45 µm is chosen. At this length, there is a 50:50 splitting of optical power around 1530 nm for both modes. Applying 35 mW of power shifts the 50:50 splitting of optical power for both TE0 and TE1 modes to 1550 nm.

4.5 Summary

This chapter introduces a mode-selective tunable directional coupler (MS-TDC) capable of selectively coupling the TE1 mode with varying coupling ratios by adjusting the electrical power applied to the heater above the coupling waveguides. The TE0 mode continues to pass entirely through the through port. The coupler has dimensions with a width of 800 nm to support both TE0 and TE1 modes and a gap of 160 nm, with crossover lengths of 13.5 µm for the TE1 mode and 145 µm for the TE0 mode. The MS-TDC can serve as a building block to integrate higher-order optical modes into reconfigurable optical processors (ROPs) and as a component within on-chip mode-division multiplexing (MDM) systems. It functions as a TE0/TE1 mode (de)multiplexer, offering tunability to correct errors and variations resulting from fabrication.

Our experiments validate a tunability of up to 10% in the splitting ratio for a coupling length of 6.5 µm, and a tunability of 25% for a coupling length of 23 µm when applying power in the range of 0 to 45 mW. This enhanced tunability aligns with the theory that it is directly linked to the increased length of the coupling waveguides, following a sinusoidal

form. Theoretically, increasing the coupling length to 40 µm while maintaining the same heater dimensions and power rating could enhance tunability up to 35%.

Finally, two additional TDC designs are introduced and simulated for further research to enhance control over TE modes: the design of a TE0 mode-selective 3 dB splitter that splits the TE0 mode by 50:50 while allowing the TE1 mode to propagate entirely through the through port, and the design of a 3 dB splitter for both modes, splitting both TE0 and TE1 modes by 50:50.

Chapter 5

Conclusion

In this thesis, two distinct types of tunable directional couplers were developed, each integrating a thermo-optic phase shifter to precisely adjust the effective refractive index of the coupling region, thus enabling fine-tuning of the coupling ratio. Both designs were comprehensively studied through design, simulation, experimentation, and validation processes. These couplers served dual purposes. They addressed fabrication process variations that often lead to splitting ratio inaccuracy errors in directional couplers, affecting accuracy in optical computing applications like reconfigurable optical processors (ROPs). Additionally, they enabled the selective combination and separation of TE0 and TE1 modes in on-chip mode-division multiplexing (MDM) systems.

Chapter 2 delved into the theory of the thermo-optic effect, exploring the derivation of a linear relationship between the wavelength shift of the coupler 50:50 splitting point ($\Delta\lambda$) and

the change in temperature of the coupling region (ΔT). This relationship was further proven to be linear with the applied power to the metal. Additionally, the directional couplers' supermode approach for both TE0 and TE1 modes was discussed.

Detailed discussions on Mach-Zehnder interferometers (MZIs) as building blocks for reconfigurable optical processors (ROPs) followed, focusing on the MZI unitary transformation matrix and how to expand this principle to configure Reck and Clements topologies. The effect of a 2% inaccuracy in directional coupler splitters in MZIs that build a 4×4 Reck topology was also examined. Simulation results showed that 63% of the topology elements exhibited errors greater than 2%, and two elements exhibited a significant 6% loss of accuracy.

In Chapter 3, a single-mode tunable directional coupler (SM-TDC) that exclusively propagates and tunes the coupling ratio for the TE0 mode was experimentally demonstrated. The linear relationship between electrical power and the wavelength shift in the splitting ratio of the couplers was experimentally validated, confirming that the wavelength shift always occured towards longer wavelengths, in a manner similar to reducing the coupling length. By employing a coupler with a 50 µm heater length and a 6.5 µm coupling length, a 10% tunability range in the splitting percentage was achieved experimentally when varying the power from 0 to 45 mW. Furthermore, in simulation a threefold improvement in tunability was attained with a heater length of 10 µm, surpassing the typical fabrication-induced splitting deviations in SOI directional couplers. To design a

TDC that achieves a specific splitting ratio at a desired wavelength, the design should target that splitting ratio at a slightly shorter wavelength (corresponding to a longer coupling length). At the same time, it should exhibit a 3% to 4% deviation from that splitting ratio at the desired wavelength before applying power. This deviation should exceed the possible fabrication-induced variations in SOI directional couplers, which typically fall within the range of ±2% to ±3%.

In Chapter 4, a mode-selective tunable directional coupler capable of propagating both TE0 and TE1 modes, and selectively coupling a specific percentage of TE1 mode power while bypassing all of the TE0 mode, was experimentally demonstrate. First, a design capable of achieving a 50:50 split for TE1 while bypassing TE0 for ROP applications was validated through two coupling lengths. For a 6.5 µm coupling length, a 10% tunability range in the splitting percentage was achieved, and for a 23 µm coupling length, a 25% tunability was demonstrated when varying power from 0 to 45 mW for a 50 µm heater length. Theoretically, this tunability is enhanced to 35% with a coupling length of 40 µm. The performance improvement in the range of tunability for the same power rating and heater length is due to the increase in the coupler length. Second, a design capable of complete separation of TE0 and TE1 modes for on-chip MDM systems was presented, and the concept was validated through simulation. Tunable full mode separation was achieved by changing the length of the coupling waveguides to 15 µm with 30 mW applied power. Theoretically, with a coupling length of 30 µm, complete transfer of the TE1 mode from the output through port to the

output cross port was achieved by applying 260 mW, while the TE0 mode optical power was directed through the through port.

Lastly, in Chapter 4, two future research directions in tunable directional couplers were presented to further enhance and refine the control over TE modes. Firstly, the design of a TDC capable of achieving a 50:50 splitting ratio for TE0 mode while bypassing all TE1 mode in the through port was discussed and simulated. Next, the design of a TDC capable of splitting both TE0 and TE1 modes with a 50:50 splitting ratio was proposed and simulated. This design holds promising potential for the development of two-mode ROPs. This is particularly relevant given the recent demonstration of a mode-selective phase shifter in an MZI that can manipulate both TE0 and TE1 modes. Additionally, applied electrical power simulations for both proposed designs were conducted to validate their tunability for fabrication process variations.

Overall, this thesis made significant contributions to the field of mode-selective directional couplers by providing valuable insights and advancements in the design, simulation, and experimental validation of tunable directional couplers. These developments enabled precise control over TE modes in a range of optical applications.

Bibliography

[1] Z. Chen and M. Segev, "Highlighting photonics: looking into the next decade," *eLight*, vol. 1, no. 1, Jun. 2021, doi: 10.1186/s43593-021-00002-y.

[2] J. Mower, N. C. Harris, G. R. Steinbrecher, Y. Lahini, and D. Englund, "High-fidelity quantum state evolution in imperfect photonic integrated circuits," *Physical Review A*, vol. 92, no. 3, Sep. 2015, doi: 10.1103/physreva.92.032322.

[3] F. Shokraneh, M. S. Nezami, and O. Liboiron-Ladouceur, "Theoretical and Experimental Analysis of a 4 × 4 Reconfigurable MZI-Based Linear Optical Processor," *Journal of Lightwave Technology*, vol. 38, no. 6, pp. 1258–1267, Mar. 2020, doi: 10.1109/jlt.2020.2966949.

[4] B. J. Shastri, *et al.*, "Photonics for artificial intelligence and neuromorphic computing," *Nature Photonics*, vol. 15, no. 2, pp. 102–114, Jan. 2021, doi: 10.1038/s41566-020-00754-y.

[5] T. Wang, S.-Y. Ma, L. G. Wright, T. Onodera, B. C. Richard, and P. L. McMahon, "An optical neural network using less than 1 photon per multiplication," *Nature Communications*, vol. 13, no. 1, Jan. 2022, doi: 10.1038/s41467-021-27774-8.

[6] M. Reck, A. Zeilinger, H. J. Bernstein, and P. Bertani, "Experimental realization of any discrete unitary operator," *Physical Review Letters*, vol. 73, no. 1, pp. 58–61, Jul. 1994, doi: 10.1103/physrevlett.73.58.

[7] M. Y.-S. Fang, S. Manipatruni, C. Wierzynski, A. Khosrowshahi, and M. R. DeWeese, "Design of optical neural networks with component imprecisions," *Optics Express*, vol. 27, no. 10, pp. 14009-14029, 2019, doi: 10.1364/OE.27.014009.

[8] K. R. Mojaver, S. M. R. Safaee, S. S. Morrison and O. Liboiron-Ladouceur, "Recent Advancements in Mode Division Multiplexing for Communication and Computation in Silicon Photonics," *Journal of Lightwave Technology*, doi: 10.1109/JLT.2024.3412391.

[9] K. R. Mojaver and O. Liboiron-Ladouceur, "On-Chip Optical Phase Monitoring in Multi-Transverse-Mode Integrated Silicon-Based Optical Processors," *IEEE Journal of Selected Topics in Quantum Electronics*, vol. 28, no. 6: High Density Integr. Multipurpose Photon. Circ., pp. 1-7, Nov.-Dec. 2022, Art no. 6101207, doi: 10.1109/JSTQE.2022.3209023.

[10] D. J. Richardson, J. M. Fini, and L. E. Nelson, "Space-division multiplexing in optical fibres," *Nature Photon.*, vol. 7, pp. 354–362, May 2013, doi: 10.1038/nphoton.2013.94.

[11] A. A. Aboketaf, A. W. Elshaari, and S. F. Preble, "Optical time division multiplexer on silicon chip," *Optics Express*, vol. 18, no. 13, p. 13529, Jun. 2010, doi: 10.1364/oe.18.013529.

[12] X. Fu, H. Jia, S. Shao, X. Fang, L. Zhang and L. Yang, "Silicon Photonic Wavelength (De-)Multiplexer for Low-loss Flat-passband DWDM Applications," *2018 Asia Communications and Photonics Conference (ACP)*, Hangzhou, China, 2018, pp. 1-2, doi: 10.1109/ACP.2018.8596123.

[13] T. Kanai, R. Koma, J. -I. Kani and T. Yoshida, "Future Long-Reach Optical Access Network with Digital Coherent Technologies," *Conference on Lasers and Electro-Optics (CLEO)*, San Jose, CA, USA, 2021, pp. 1-2, doi: 10.1364/cleo_si.2021.sth1i.5.

[14] R.-J. Essiambre, G. Kramer, P. J. Winzer, G. J. Foschini, and B. Goebel, "Capacity Limits of Optical Fiber Networks," *Journal of Lightwave Technology*, vol. 28, no. 4, pp. 662–701, Feb. 2010, doi: 10.1109/jlt.2009.2039464.

[15] R. Liu, H. Li, W. Zhao, M. Zhu, G. Li and D. Dai, "Supermode-Division-(de)Multiplexing With a Multi-Core Silicon Photonic Bus Waveguide," *Journal of Lightwave Technology*, vol. 42, no. 9, pp. 3330-3337, May. 2024, doi: 10.1109/JLT.2024.3354811.

[16] W. Zhang, H. Ghorbani, T. Shao and J. Yao, "Mode-Division Multiplexed PAM-4 Signal Transmission in a Silicon Photonic Chip," *2019 International Topical*

Meeting on Microwave Photonics (MWP), Ottawa, ON, Canada, 2019, pp. 1-4, doi: 10.1109/MWP.2019.8892155.

[17] B. Behera, S. Varshney and M. N. Mohanty, "Demonstration of a 4×3×10 Gbps WI-WDM Transmission Over MDM Link Using Ring-Core FMF" *Advances in Intelligent Computing and Communication*, Springer, pp. 601-610, 2021, doi: 10.1007/978-981-16-0695-3_56.

[18] K. R. Mojaver, "SiPh_MDM_PDK," GitHub, Jun. 27, 2023. [Online]. Available: `https://github.com/KavehMojaver/SiPh_MDM_PDK`.

[19] D. J. Thomson, Y. Hu, G. T. Reed and J. -M. Fedeli, "Low Loss MMI Couplers for High Performance MZI Modulators,"*IEEE Photonics Technology Letters*, vol. 22, no. 20, pp. 1485-1487, Oct.15, 2010, doi: 10.1109/LPT.2010.2063018.

[20] D. A. B. Miller, "Perfect optics with imperfect components," *Optica*, vol. 2, no. 8, p. 747, Aug. 2015, doi: 10.1364/optica.2.000747.

[21] S. Bandyopadhyay, R. Hamerly, and D. Englund, "Hardware error correction for programmable photonics," *Optica*, vol. 8, no. 10, pp. 1247-1255, Sep. 2021, doi: 10.1364/optica.424052.

[22] Y. Ding, J. Xu, F. Da Ros, B. Huang, H. Ou, and C. Peucheret, "On-chip two-mode division multiplexing using tapered directional coupler-based mode multiplexer

and demultiplexer,"*Optics Express*, vol. 21, no. 8, p. 10376, Apr. 2013, doi: 10.1364/oe.21.010376.

[23] J. Liao, *et al.*, "Mode Splitter Without Changing the Mode Order in SOI Waveguide," *IEEE Photonics Technology Letters*, vol. 28, no. 22, pp. 2597-2600, 15 Nov.15, 2016, doi: 10.1109/LPT.2016.2606496.

[24] D. Dai, Z. Wang, and J. E. Bowers, "Ultrashort broadband polarization beam splitter based on an asymmetrical directional coupler," *Optics Letters*, vol. 36, no. 13, pp. 2590–2590, Jul. 2011, doi: 10.1364/ol.36.002590.

[25] D. A. Antoniadis, "SOI CMOS front-end technology: options and tradeoffs," *1995 IEEE International SOI Conference Proceedings*, Tucson, AZ, USA, 1995, pp. 1-3, doi: 10.1109/SOI.1995.526431.

[26] R. Baets, *et al.*, "Silicon photonics: Silicon nitride versus silicon-on-insulator," *Optical Fiber Communications Conference and Exhibition (OFC)*, Anaheim, CA, USA, pp. 1-3, Mar. 2016, doi: 10.1364/OFC.2016.Th3J.1.

[27] J. Komma, C. Schwarz, G. Hofmann, D. Heinert, and R. Nawrodt, "Thermo-optic coefficient of silicon at 1550 nm and cryogenic temperatures," *Applied Physics Letters*, vol. 101, no. 4, p. 041905, Jul. 2012, doi: 10.1063/1.4738989.

[28] M. Nedeljkovic, *et al.*, "Mid-Infrared Thermo-Optic Modulators in SoI," *IEEE Photonics Technology Letters*, vol. 26, no. 13, pp. 1352-1355, July1, 2014, doi: 10.1109/LPT.2014.2323702.

[29] A. Pisal and R. Henry, "Thermo-Optic switch: Device structure and design," *2016 2nd International Conference on Advances in Electrical, Electronics, Information, Communication and Bio-Informatics (AEEICB)*, Chennai, India, 2016, pp. 292-295, doi: 10.1109/AEEICB.2016.7538293.

[30] "Applied Nanotools Inc.," Applied Nanotools Inc. | X-Ray Optics and Integrated Photonics, Jan. 04, 2018. https://www.appliednt.com (accessed May 16, 2024)

[31] M. Nyakuchena, C. Juntunen, P. Shea, and Y. Sung, "Refractive index dispersion measurement in the short-wave infrared range using synthetic phase microscopy," *Physical chemistry chemical physics/PCCP. Physical chemistry chemical physics*, vol. 25, no. 34, pp. 23141-23149, Jan. 2023, doi: 10.1039/d3cp03158f.

[32] M. J. Weber, *Handbook of optical materials*. Boca Raton: CRC Press, 2003.

[33] W. D. Callister and D. G. Rethwisch, *Materials Science and Engineering: An Introduction*, 10th ed. Hoboken, Nj: Wiley, 2018.

[34] K. Gloos, C. Mitschka, F. Pobell, and P. Smeibidl, "Thermal conductivity of normal and superconducting metals," *Cryogenics*, vol. 30, no. 1, pp. 14–18, Jan. 1990, doi: 10.1016/0011-2275(90)90107-n.

[35] A. Masood,*et al.*, "CMOS-compatible Tungsten heaters for silicon photonic waveguides," *The 9th International Conference on Group IV Photonics (GFP)*, San Diego, CA, USA, 2012, pp. 234-236, doi: 10.1109/GROUP4.2012.6324144.

[36] D. Coenen, *et al.*, "Electromigration Performance Improvement of Metal Heaters for Si Photonic Ring Modulators," *IEEE Transactions on Device and Materials Reliability*, vol. 22, no. 3, pp. 417-423, Sept. 2022, doi: 10.1109/TDMR.2022.3187822.

[37] C. R. Pollock and M. Lipson, Integrated photonics. Norwell, Mass.: Kluwer Academic, 2010.

[38] L. Zhu and J. Sun, "Silicon-based wavelength division multiplexer by exploiting mode conversion in asymmetric directional couplers," *OSA Continuum*, vol. 1, no. 1, p. 92-103, Sep. 2018, doi: 10.1364/osac.1.000092.

[39] W. K. Zhao, K. X. Chen, J. Y. Wu and K. S. Chiang, "Horizontal Directional Coupler Formed With Waveguides of Different Heights for Mode-Division Multiplexing," *IEEE Photonics Journal*, vol. 9, no. 5, pp. 1-9, Oct. 2017, Art no. 6601509, doi: 10.1109/JPHOT.2017.2731046.

[40] L. Chrostowski and M. Hochberg, *Silicon Photonics Design: From Devices to Systems.* Cambridge: Cambridge University Press, 2015.

[41] N. Kumar, M. R. Shenoy, K. Thyagarajan, and B. P. Pal, "Graphical Representation of the Supermode Theory of a Waveguide Directional Coupler," *Fiber and Integrated Optics*, vol. 25, no. 3, pp. 231–244, Jul. 2006, doi: 10.1080/01468030600569925.

[42] D. F. G. Gallagher and T. P. Felici, "Eigenmode expansion methods for simulation of optical propagation in photonics: pros and cons," *Proceedings of SPIE*, Jun. 2003, doi: 10.1117/12.473173.

[43] H. Mursyidah and Subiono, "Eigenvalue, eigenvector, eigenmode of reducible matrix and its application," *AIP conference proceedings*, Jan. 2017, doi: 10.1063/1.4994447.

[44] A. W. Snyder and J. D. Love, Optical Waveguide Theory. Springer Science & Business Media, 2012.

[45] K. Okamoto, Fundamentals of optical waveguides. London ; San Diego, Ca: Academic Press, 2022.

[46] M. Spivak, Calculus on Manifolds : A Modern Approach To Classical Theorems Of Advanced Calculus. Boca Raton, FL: CRC Press, 2018.

[47] T. W. Hughes, Momchil Minkov, Y. Shi, and S. Fan, "Training of photonic neural networks through in situ backpropagation and gradient measurement," *Optica*, vol. 5, no. 7, pp. 864–864, Jul. 2018, doi: 10.1364/optica.5.000864.

[48] J. C. Mikkelsen, W. D. Sacher and J. K. S. Poon, "Dimensional variation tolerant silicon-on-insulator directional couplers", *Optics Express*, vol. 22, no. 3, pp. 3145-3150, 2014, doi: 10.1364/oe.22.003145.

[49] W. R. Clements, P. C. Humphreys, B. J. Metcalf, W. S. Kolthammer, and I. A. Walsmley, "Optimal design for universal multiport interferometers," *Optica*, vol. 3, no. 12, p. 1460, Dec. 2016, doi: 10.1364/optica.3.001460.

[50] D. A. Miller, "Self-configuring universal linear optical component", *Photonics Research*, vol. 1, no. 1, pp. 1-15, 2013, doi: 10.1364/PRJ.1.000001.

[51] Z. J. Zawistowski and B. Jaskorzynska, "Electrically tunable filter based on directional coupler with 1D photonic crystal arm infiltrated with smectic liquid crystal," Proceedings of 2004 6th International Conference on Transparent Optical Networks (IEEE Cat. No.04EX804), Wroclaw, Poland, 2004, pp. 127-130 vol.2, doi: 10.1109/ICTON.2004.1361985.

[52] Q. Huang, K. S. Chiang, and W. Jin, "Thermo-optic switchable mode multiplexer based on cascaded vertical waveguide directional couplers," *2017 Opto-Electronics*

and Communications Conference (OECC) and Photonics Global Conference (PGC), Singapore, 2017, pp. 1-2, doi: 10.1109/OECC.2017.8115003.

[53] W. K. Zhao, K. X. Chen, and J. Y. Wu, "Broadband Mode Multiplexer Formed With Non-Planar Tapered Directional Couplers," *IEEE Photonics Technology Letters*, vol. 31, no. 2, pp. 169–172, Jan. 2019, doi: 10.1109/LPT.2018.2887352.

[54] H. Yun, Z. Lu, Y. Wang, W. Shi, L. Christowski and N. A. F. Jaeger, "2×2 Broadband adiabatic 3-dB couplers on SOI strip waveguides for TE and TM modes," *2015 Conference on Lasers and Electro-Optics (CLEO)*, San Jose, CA, USA, 2015, pp. 1-2, doi: 10.1364/CLEO_SI.2015.STh1F.8.

[55] A. Y. Takabayashi, *et al.*, "Compact Integrated Silicon Photonic MEMS Power Coupler For Programmable Photonics," *2022 IEEE 35th International Conference on Micro Electro Mechanical Systems Conference (MEMS)*, Tokyo, Japan, 2022, pp. 216-219, doi: 10.1109/MEMS51670.2022.9699708.

[56] T. Y. Teo, M. Krbal, J. Mistrik, J. Prikryl, L. Lu, and R. E. Simpson, "Comparison and analysis of phase change materials-based reconfigurable silicon photonic directional couplers," *Optical Materials Express*, vol. 12, no. 2, pp. 606-621, Jan. 2022, doi: 10.1364/ome.447289.

[57] L. Martin-Monie, *et al.*, "Endurance of chalcogenide optical phase change materials: a review," *Optical Materials Express*, vol. 12, no. 6, pp. 2145–2145, Mar. 2022, doi: 10.1364/ome.456428.

[58] P. Orlandi, F. Morichetti, M. J. Strain, M. Sorel, A. Melloni, and P. Bassi, "Tunable silicon photonics directional coupler driven by a transverse temperature gradient," *Optics Letters*, vol. 38, no. 6, p. 863, Mar. 2013, doi: 10.1364/ol.38.000863.

[59] D. Pérez-López, A. María, E. Sánchez, P. DasMahapatra, and J. Capmany, "Integrated photonic tunable basic units using dual-drive directional couplers," *Optics Express*, vol. 27, no. 26, pp. 38071–38071, Dec. 2019, doi: 10.1364/oe.27.038071.

[60] S. M. R. Safaee, K. R. Mojaver, D. Gostimirovic and O. Liboiron-Ladouceur, "Experimentally validated simulation of a mode-sensitive thermo-optic phase-shifter," 49th European Conference on Optical Communications (ECOC 2023), Hybrid Conference, Glasgow, UK, 2023, pp. 1406-1409, doi: 10.1049/icp.2023.2571.

[61] C. Zhao, L. Xu, and L. Liu, "Ultrahigh Sensitivity Mach-Zehnder Interferometer Sensor Based on a Weak One-Dimensional Field Confinement Silica Waveguide," Sensors, vol. 21, no. 19, pp. 6600–6600, Oct. 2021, doi: 10.3390/s21196600.